Utrecht University
Faculty of Science

Department of Theoretical Physics

Utrecht University

Master Thesis

submitted for the degree of

Master's Degree in Theoretical Physics

Topological Phases of Interacting Parafermions

"An exploration of the quantum phases of strongly correlated parafermion chains"

by

Juan José Rodríguez Aldavero

Submission Date: February 8, 2023
Supervisors: Dr Dirk Schuricht
Dr Lars Fritz

Topological Phases of Interacting Parafermions

"An exploration of the quantum phases of strongly correlated parafermion chains"

Juan José Rodríguez Aldavero

Abstract

Parafermion chains are one-dimensional, quantum many-body systems which show topological phases possessing intriguing properties. For example, they are able to host quasiparticles with exotic quantum statistics called non-Abelian anyons. Unlike bosons or fermions, the exchange statistics shown by anyons allows them to modify the state of the system they are contained in. While Abelian anyons induce a phase change on the quantum system when they are spatially exchanged, non-Abelian anyons induce unitary transformations, which allows for the development of applications in fields such as quantum computing.

In this thesis, the properties of increasingly complex parafermion chains are analysed. The starting point is given by the Kitaev model and its corresponding spin chain, the quantum Ising model. Afterwards, its generalizations lead to the discussion of the 3-state Potts model and the corresponding parafermion chain. Finally, the models are further generalized by adding extension terms on their respective Hamiltonians. Many of these models are very challenging to approach by means of analytical methods due to the presence of strong interactions, so their phase transitions are characterised by means of numerical methods based on tensor network ansätzen such as the Density Matrix Renormalization Group (DMRG) or the Multi-Scale Entanglement Renormalization Ansatz (MERA). The data is then analysed and interpreted using techniques coming from conformal field theory, finite-size scaling or the real-space renormalization group.

The aim of this thesis is to characterize a region of the phase diagram of a generalized parafermion chain with two extension terms. A strong emphasis will be placed on the phase transition given between the trivial and $\mathbb{Z}_3$-ordered topological phases, as well as on a feature shown by the topological phase: a parametrized line on which the system is frustration-free. Along this line, the ground state of the system can be constructed exactly for arbitrarily large systems and exhibits exact degeneracy, even in the presence of strong interactions, paving the way for a more precise analysis of the topological properties of these kinds of models.

Acknowledgements

I would like to thank my family for their support during the last two years that I have been studying this Masters in Utrecht. Dad, Mom and Ari, thanks so much for always being there and for your unconditional love. Also, I would like to thank my partner for her support and patience during my time in Utrecht. Tam, I know that these years have seemed like such a long time, but I appreciate that you have still been waiting for me. It means a lot to me.

Thanks as well to the various people whose help has made this thesis possible. I would like to acknowledge the work of Dr Jurriaan Wouters and collaborators in the study of parafermion chains as this thesis is mainly an extension of their work *Phase diagram of an extended parafermion chain* [1], in which they give a thorough explanation of the methods and techniques required to tackle parafermion chains. I would also like to thank Jurriaan for the help he gave me at the beginning of the thesis when I was facing some difficulties.
I would also like to thank Dr Lars Fritz, Dr Mikael Fremling and the rest of the research group for the very interesting discussions given at the weekly meetings. I have found them very informative and interesting. Thanks as well to Dr Hosho Katsura for his help in understanding the interpolation model approached in the appendix of this work as well as for the interesting discussions.

Finally, I would like to thank my thesis supervisor, Dr Dirk Schuricht, for his guidance over the past year. His expertise and insights have been invaluable in completing this thesis. I appreciate the time and energy he has invested in me and in this project, and I am grateful for the opportunity to work under his supervision on this fascinating topic.

Sincerely,
Juanjo

Declaration

I, Juan José Rodríguez, declare that this thesis *Topological Phases of Interacting Parafermions* and the work presented in it are my own. I confirm that:

- This work was done wholly or mainly while in candidature for a research degree at this University.
- Where any part of this thesis has previously been submitted for a degree or any other qualification at this University or any other institution, this has been clearly stated.
- Where I have consulted the published work of others, this is always clearly attributed.
- Where I have quoted from the work of others, the source is always given. With the exception of such quotations, this thesis is entirely my own work.
- I have acknowledged all main sources of help.
- Where the thesis is based on work done by myself jointly with others, I have made clear exactly what was done by others and what I have contributed myself.

Signed:

Date:

Preface

Topological phases of matter have become of increasing interest in the last decades. The number of quantum systems exhibiting topological phases is growing rapidly, and their exotic properties are of interest both for the theoretical insights they provide as well as for their potential applications. Examples of quantum systems with topological phases include quantum spin liquids, topological insulators, Dirac semimetals and topological superconductors, among many others. In this work, we will focus on a class of topological superconductors receiving the name of parafermion chains.

One of the canonical models showing a topological phase is the Kitaev model. Consisting of a one-dimensional chain of interacting fermions, this model manifests some of its topological properties in the form of two quantum states, called Majorana edge modes, located at its ends. They receive their name because their associated quasiparticles are their own antiparticle, and this implies that they pose no effect on the total energy of the model. Also, their exchange statistics is not equivalent to the one of bosons or fermions, but to so-called non-Abelian anyons because they give rise to unitary transformations over the whole quantum system when they are spatially exchanged. This property is expected to play an important role in the development of future applications in domains such as quantum computing, in order to process or store quantum information.

However, while the properties of Majorana zero modes are appealing, they are limited by the fact that they do not support the realization of an arbitrary unitary transformation. This limitation can be overcome by generalising the fermionic degrees of freedom of the Kitaev model, leading to entities called parafermions. These new degrees of freedom yield edge modes which exhibit non-Abelian statistics that do not have this limitation and can indeed realize arbitrary unitary transformations. This is one of the many reasons why intensive effort has been devoted to better understanding parafermion chains in recent years.

In this work we will analyse the phase transitions and corresponding phase diagram of extended parafermion chains. Their strong interactions largely prohibit their analytical treatment, so most of the analysis will be carried out using numerical methods such as tensor networks ansätzen which assume a certain simplified structure on the quantum states of the system. This work will conclude with the analysis of a twice-extended parafermion chain, motivated by the fact that its associated three-dimensional phase diagram contains a parametrised line along which the system is frustration-free. This means that its ground state can be computed exactly, regardless of the strong correlations involved.

This thesis will follow the outline shown below:

1. The first section will be dedicated to the introduction of concepts related to quantum computing, it being an important motivator for the study of parafermion chains. We will see why it is needed to overcome some of the limitations shown by classical computers, as well some of its own limitations which can be potentially overcome by the exploitation of the topological properties of quantum matter.

2. The second section will introduce some concepts related to the topological phases of quantum matter, as well as some analytical techniques that can be used to characterize them. While strongly correlated quantum systems can only be solved analytically in a limited number of cases, there are techniques that facilitate the analysis of their phase diagram, such as the renormalization group; and interpretation of numerical data, such as the conformal field theory and finite-size scaling.

3. In the third section we will focus on the numerical methods used to deal with strongly correlated systems. In particular, we will look at a category of methods that rely on a large simplification of the quantum states by assuming that their structure takes the form of a contraction of a network of tensors. We will see how there are several possible structures within this class of methods, the simplest being a product of matrices, and also how they need to be accompanied with a variational algorithm in order to optimise them and bring them as close as possible to the actual states, some of the most popular being DMRG and MERA.

4. In the fourth section the Kitaev model will be reintroduced as the starting point for the development of parafermions models. We will discuss its mathematical structure such as its duality with the quantum Ising model, as well as some of its properties. We will then examine the conformal field theory associated with its quantum phase transition, as well as the applications of its topological properties in quantum computing, manifested as Majorana edge modes. Finally, being an analytically solvable model, we will use it as a benchmark by testing the numerical methods that will be used in the following chapters.

5. In the fifth section we will introduce the Potts model as a generalization of the quantum Ising model, and then explore its dual form as a parafermion chain by means of an appropriate transformation. We will discuss the consequences of this generalisation, such as it becoming analytically intractable and the need for numerical methods, as well as how their associated parafermionic edge modes overcome the limitations shown by Majorana edge modes when trying to develop applications in quantum computing.

6. In the sixth section we will generalize the parafermion chain by introducing an extension term in the Hamiltonian of the Potts model, arriving at the ANNNP model. This generalization, motivated by a potential experimental realization of the model, results in an enlarged phase diagram which will be explored and discussed.

7. In the seventh section we will introduce another generalization in the parafermion chain by incorporating an extension term into the ANNNP Hamiltonian. This extension is motivated by the emergence of a parametrised Peschel-Emery line along which the system becomes frustration-free. We will discuss the analytical basis for this line and study the extension of the phase diagram along this new dimension in order to characterise the nature of the phase transition shown along it.

8. Finally, the eighth section summarises the numerical results obtained, poses open questions and discusses possible generalisations of this work for future iterations.

In addition, we will present in the Appendix an alternative one-dimensional quantum model that was studied during the course of this work by means of the same numerical and analyticall methods. In this way we will show how the approach followed in this work is broadly applicable within the domain of one-dimensional quantum many-body systems.

Contents

1 The quantum computer **9**
- 1.1 The Classical Computer . . . 9
- 1.2 The Quantum Computer . . . 10

2 Topological quantum matter **15**
- 2.1 Topological quantum computing . . . 15
- 2.2 Topological invariants and symmetry . . . 16
- 2.3 Conformal field theory . . . 18
- 2.4 The renormalization group . . . 25
- 2.5 Finite-size scaling . . . 30

3 Numerical methods **32**
- 3.1 Exact diagonalization . . . 32
- 3.2 Tensor networks . . . 33
- 3.3 The density matrix renormalization group . . . 35
- 3.4 The multi-scale entanglement renormalization ansatz . . . 39

4 The Kitaev model **41**
- 4.1 Introduction . . . 41
- 4.2 The Jordan-Wigner transformation . . . 43
- 4.3 Analytical solution . . . 44
- 4.4 Numerical results at the phase transition . . . 46
- 4.5 Non-Abelian statistics and quantum computation . . . 47
- 4.6 Interactions: the ANNNI model . . . 50

5 The parafermion chain **52**
- 5.1 Introduction . . . 52
- 5.2 The Fradkin-Kadanoff transformation . . . 54
- 5.3 Numerical results at the phase transition . . . 55
- 5.4 Non-Abelian statistics and quantum computation . . . 57

6 The parafermion chain with one extension **58**
- 6.1 Introduction . . . 58
- 6.2 The Fradkin-Kadanoff transformation . . . 59
- 6.3 Phase diagram . . . 59
- 6.4 Numerical results at the phase transition . . . 60
- 6.5 Non-Abelian statistics and quantum computation . . . 63

7 The parafermion chain with two extensions **65**
7.1 Introduction . . . 65
7.2 Numerical results at the phase transition . . . 66
7.3 The Witten conjugation argument . . . 71
7.4 Frustration-free effects . . . 73
7.5 Phase diagram . . . 74

8 Discussion **77**
8.1 Possible extensions . . . 78

A Study of a parametric interpolation between the Sutherland and the quantum torus chain models **79**
A.1 Introduction . . . 79
A.2 Results . . . 81
A.3 Discussion . . . 85

B Out-of-scope numerical data **86**

1 The quantum computer

In this chapter, we will briefly present the classical computer as a way to motivate the major efforts being made to develop a fault-tolerant quantum computer. In particular, we will look at how quantum computers are able to deal with problems that were previously thought to be classically intractable, and which promise very interesting applications in various fields of science and technology.

We will then present some general features of quantum computing and the main challenge facing its development: the correction of errors due to the quantum decoherence of its qubits.

Finally, we will use this problem as a way to motivate the paradigm of topological quantum computing for fault-tolerant quantum computing. This approach is related to the topic of this thesis, namely parafermion chains, because it can be experimentally realized by exploiting the topological properties of these quantum systems.

1.1 The Classical Computer

The society in which we live has been profoundly transformed in recent decades by the development of the computer. Since its inception in the mid-20th century, the computer has been gradually introduced worldwide, bringing with it many advances that have changed the way we live our daily lives.

The *father* of the computer was arguably the English mathematician Alan Turing, who developed the concept of the Universal Computing Machine in his 1936 paper *On Computable Numbers* [2]. It described what is now known as the Turing machine, an abstract entity capable of performing computations and **algorithms**. This was followed in 1947 by the introduction of the transistor, which laid the physical foundations of the modern computer. This device, invented by the physicists John Bardeen and Walter Brattain, uses the properties of a semiconductor material to modify its own conductivity in response to an external input, such as an electrical voltage [3]. This makes it possible to develop logic gates on binary language (bits), which in turn gives rise to integrated circuits and, ultimately, the computer processor.

A computer is essentially a machine that can execute algorithms. This means that it is capable of executing a series of very simple instructions, one after the other, to solve a

particular problem. The difficulty of solving a computational problem can be expressed mathematically by the computational complexity of the corresponding algorithm. Its time complexity can be defined as the ratio between the time required to solve the problem and its *size*. One way of expressing this complexity is in big-O notation, which expresses the asymptotic functional dependence of the time to complete on the problem size, for the worst case. For example, the problem of sorting a list of integers $[i_1, \ldots, i_n]$ from smallest to largest can be tackled with an algorithm whose time complexity is $\mathcal{O}(n \log n)$, where n are the elements in the list, i.e. it can take *at most* $n \log n$ steps. Computational complexity in turn defines **complexity classes** [4], which are very useful constructs for discerning whether a computational problem is tractable or not. The class **P** is defined as the set of problems for which there is known to be an algorithm whose time complexity is polynomial in the problem size and verifiable in polynomial time. Then they are said to run in polynomial time and are assumed to be tractable in principle. On the other hand, the class **NP** is defined as the set of problems for which there is no known algorithm that runs in polynomial time, although they are verifiable in polynomial time, and are therefore considered intractable. An example of this is the decomposition of a very large integer into its prime factors, since the best available algorithm for solving it has almost exponential computational complexity, but given a solution (a set of primes) it is easy to check that these are the factors you are looking for. This special property of large integers underlies many modern cryptographic methods that protect our communications.

One of the most remarkable facts about computers is the rate at which their computing power has increased in recent years. Since the discovery of the transistor, a massive effort has been made to reduce its size as much as possible in order to pack as many of them into computer processors as possible. The empirical manifestation of this is known as Moore's Law, which states that the density of transistors in a processor doubles every two years. This exponential growth has continued for several decades, resulting in computing power that would have been unimaginable just a few decades ago.

However, the scale of today's transistors is already on the order of a few atoms, and it is therefore believed that Moore's Law will soon cease to hold (with some companies claiming that it is actually no longer holding). This limitation, together with the fact that there is a large class of problems in the **NP** class that are intractable, makes it clear that classical computers have shortcomings. An emerging technology that promises to overcome (some of) these weaknesses is quantum computing, which uses the laws of quantum physics to process information in a fundamentally different way, and which promises some very significant improvements.

1.2 The Quantum Computer

The laws of quantum mechanics, on which much of physics is founded, are far removed from human intuition. Their probabilistic foundations, theoretically formulated by physicists such as Schrödinger or Heisenberg in the first quarter of the 20th century, give rise to "strange" phenomena such as superposition of states, quantum entanglement or quantum teleportation [4].

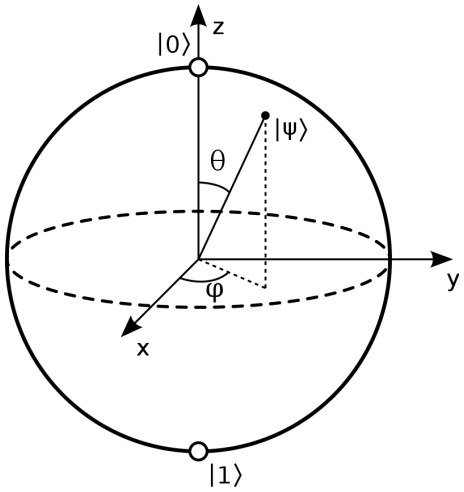

Figure 1.1: Bloch sphere representation of a qubit.

Not long after the formulation of quantum mechanics was completed, physicists began to consider its application to the field of computing. In 1982, for example, the famous physicist Richard Feynman postulated that the best device for simulating quantum systems would be a **quantum computer** [5]. However, the real awakening of interest in quantum computing came at the end of the 20th century thanks to Peter Shor, who was able to develop one of the first quantum algorithms with real applications [6]. As a result, the interest in developing a quantum computer has grown over the last 25 years.

One of the fundamental concepts of quantum computing is to discard bit-based binary logic in favour of a much richer one. This is achieved by introducing the **qubit** (quantum bit) as a replacement for the bit. It is a binary quantum state that can be expressed mathematically as

$$|\Psi\rangle = \alpha\,|0\rangle + \beta\,|1\rangle\,, \tag{1.1}$$

where both $|0\rangle$ and $|1\rangle$ are quantum states that can be seen as the basis of a vector space known as the Hilbert space $\mathscr{H}$. Due to the normalisation of such a quantum state, i.e. $\langle\Psi|\Psi\rangle = 1$, it is possible to introduce a spherical representation called the Bloch sphere in terms of the two parameters θ and ϕ, as follows

$$|\Psi\rangle = \cos(\theta/2)\,|0\rangle + e^{i\phi}\sin(\theta/2)\,|1\rangle\,. \tag{1.2}$$

This representation can be thought of as a hollow sphere, with each point on its surface corresponding to a different quantum state, as shown in Figure 1.1.

One of the advantages of quantum superposition is that qubits can be superposed, resulting in a state or wave function that exists in a much larger Hilbert space. The number of basis states in the Hilbert space $\mathscr{H}$ of the wave function grows exponentially as 2^n, where n is the number of qubits in the system, and this wave function can be in an arbitrary superposition of all of them as

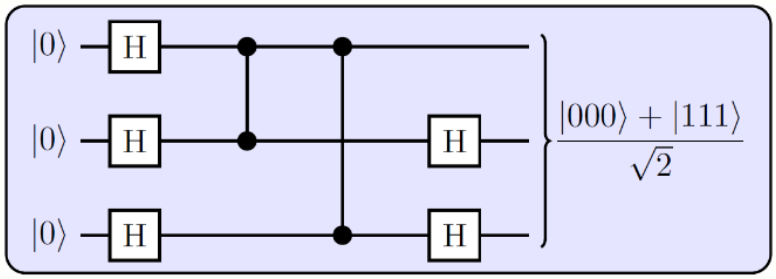

Figure 1.2: Example of a quantum circuit involving Hadamard an CZ gates, and resulting in a final three-qubit wave function.

$$|\Psi\rangle = \sum_{i=1}^{2^n} \alpha_i |i\rangle , \tag{1.3}$$

where $i = i_1 i_2 \dots i_n$ is a bitstring of length n.

According to the principles of quantum mechanics, measuring this state leads to a collapse of the wave function into one of the 2^n basis states, with a probability given by the square of its coefficient, $|\alpha_i|^2$.

Using these principles, a quantum computer implements a **quantum algorithm** by performing sequential transformations on each of the qubits of the wave function. These transformations can be thought of as rotations within the Bloch sphere of each qubit, represented by the Figure 1.1, and are performed in such a way that the measurement of the final wave function at the end of the algorithm provides information about the problem to be solved. This can be seen most clearly in the quantum circuit representation, where an initial wave function represented by n superposed qubits is processed by applying operators to the qubits. An example of a quantum circuit with two types of qubit gates is shown in Figure 1.2. These quantum gates are mathematically represented as a unitary operator to keep the overall probability of the wave function equal to unity. Examples of quantum gates are the one-qubit Hadamard gate or the two-qubit CZ gate.

Quantum algorithms, i.e. those that can be implemented using the quantum circuits described above, have a computational complexity that is different from that of classical computers. Due to the intrinsically probabilistic nature of the measurement of the total wave function, these time complexities express the asymptotic dependence of the time to completion on the size of the problem, yielding a correct solution with a certain probability δ of the time. Typically $\delta = \frac{2}{3}$ is taken, but an arbitrarily high probability can be taken without changing the nature of the quantum algorithm. These complexities in turn give rise to complexity classes. For example, the complexity class **BQP** represents the set of problems that have an associated quantum algorithm that runs in polynomial time and yields the correct solution with a probability greater than $\frac{2}{3}$ of the time. This class of problems is formally known as "efficiently solvable on a quantum computer" [4].

However, not all problems that are intractable on classical computers are solvable on

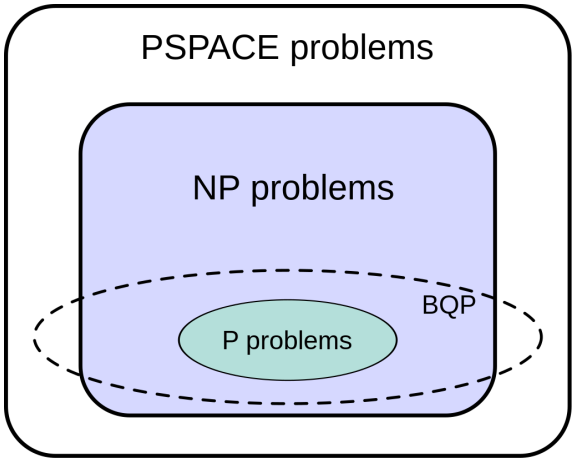

Figure 1.3: Diagram showing some of the possible complexity classes. PSPACE corresponds to the set of problems solvable using a polynomial amount of space and not necessarily verifiable in polynomial time.

quantum computers. In fact, class **BQP** represents only a small subset of all problems, which can be shown to include those of class **P** and some of class **NP**, but leaves out the vast majority, as can be seen in Figure 1.3. This fact, together with the fact that classical computers are extremely efficient at solving class **P** problems, reduces the effective utility of quantum computers to a few outstanding problems.

The paradigmatic example where a quantum computer could demonstrate an effective "supremacy" is in factoring large integers into their prime factors, since this can be tackled by **Shor's algorithm** [6]. It has a complexity of $\mathcal{O}(\log n)$, as opposed to the quasi-exponential complexity of the classical counterpart. Other promising examples can be found in the areas of quantum simulation, such as the Hamiltonian Simulation algorithm; or in the domain of numerical methods such as the HHL algorithm for solving systems of linear equations [4]. Research into new quantum algorithms is a booming and rapidly field.

Despite major efforts to build a universal quantum computer, there is currently no such device, and it is widely believed that many more years of research and development are needed. The main obstacle is the fact that the quantum wave function must remain free of unwanted external influences and noise in order for the final measurement of an algorithm to provide reliable results. The perturbation of the wave function by an external source is a phenomenon known as quantum decoherence, and it is extremely difficult to prevent. For example, a source of decoherence can be the thermal fluctuations coming from an environment temperature other than absolute zero, which can interfere with the quantum fluctuations of the wave function. For this reason, a quantum computer must be kept at temperatures as close to absolute zero as possible.

One way to address this problem is to introduce error-correcting codes into quantum algorithms. These codes would make it possible to reduce the probability of an error occurring during a quantum algorithm, at the cost of increasing the number of qubits

needed to run it. In particular, an error-correction code converts the original n physical qubits into $m < n$ error-protected logical qubits, which are the ones that are ultimately accessible by the quantum algorithm. On the other hand, the **quantum threshold theorem** states that if the error rate of the physical qubits is below a certain threshold, it is possible to set the error rate of the logical qubits to an arbitrarily low level using error correction codes [7]. For this reason, a major breakthrough in the design of a fault-tolerant quantum computer will be the discovery of a practical qubit implementation that allows their physical error rate to be reduced below this given threshold.

One possible implementation of the quantum computer exploits the topological properties of quantum matter. This implementation promises to eliminate qubit decoherence, as the quantum information would be hidden from the environment and unaffected by local perturbations. This in turn would allow the development of a fault-tolerant quantum computer without the need for error-correcting codes.

2 | Topological quantum matter

In this chapter we will discuss in more detail the properties of the topological phases of quantum matter. In particular, we will see how the topological invariants of a quantum system strongly depend on the symmetries of its Hamiltonian and how these inevitably give rise to topological properties such as edge modes. To illustrate this concept, we will consider one of the paradigmatic models of quantum matter with topological phases: the Kitaev model. This model will also serve as a starting point for the description of parafermions, and we will therefore devote an entire chapter to it later on.

We will also discuss some of the techniques available to study these systems analytically. We will see how the critical points that determine the phase transitions are characterised by a conformal field theory, and how we can study the properties of this field theory from a technique called finite-size scaling. We will also see how we can study some properties of the phase diagram of a quantum system from a set of techniques called the renormalization group. These techniques will allow us to better understand the shape of the phase diagram by studying only some of its points, and will be very useful in interpreting the numerical results.

2.1 Topological quantum computing

Topology is the branch of mathematics that studies the properties of geometric objects that are preserved under continuous transformations, called **topological invariants**. For example, one of the simplest topological invariants to conceptualise is the *genus* or number of holes in a geometric object. This quantity is conserved when the object is continuously transformed into another object. For example, as we can see in the Figure 2.1, this implies that a torus and a coffee cup are topologically equivalent, since they have only one hole.

The generalisation of this concept to quantum mechanics leads to a new definition of topological invariants, namely the mathematical quantity that is conserved when one

Figure 2.1: Topological equivalence between a torus and a coffee cup.

quantum system is continuously and arbitrarily transformed into another. When a quantum system has a non-trivial topological invariant, we say that it is in a topological phase, and this allows us to define a **topological quantum computer** as one that exploits the properties of topological phases of matter for its operation.

The study of topological phases of quantum matter is of great intrinsic interest. Some of these phases are known to exhibit quantum states at the boundaries of the system, called **edge modes**. In particular, some one-dimensional systems exhibit edge modes with special exchange statistics that do not coincide with those of bosons (the system is invariant under their exchange) or fermions (the system undergoes a π phase shift under their exchange). For this reason, the quasiparticles associated with these states are called **anyons**. If the system undergoes a phase shift under its exchange, they are called Abelian anyons, whereas if the system undergoes a more general unitary transformation, they are called **non-Abelian anyons**.

Non-Abelian anyons have applications in quantum computing, since the transformations that the system undergoes when they are spatially exchanged can represent quantum gates. These quantum gates, in turn, can implement quantum algorithms by transforming the wave function of the system in an artificially convenient way by exchanging the anyons sequentially in a process called **braiding**, following a procedure such as the one represented in Figure 1.2. Since the system experience the unitary transformations only when two of its non-Abelian anyons are exchanged, and these can be arbitrarily separated, the quantum information is immune to local perturbations and could thus allow the implementation of a fault-tolerant quantum computer.

Not all non-Abelian anyons are the same. In fact, as we will see in later chapters, there are non-Abelian anyons that only allow for a finite set of unitary transformations on the system. This means that it is not possible to approximate an arbitrary unitary transformation through a finite number of anyon braids. This hinders the development of a topological quantum computer since it prohibits it from implementing an arbitrary quantum algorithm. On the other hand, there are non-Abelian anyons that do have exchange statistics flexible enough to approximate arbitrary unitary transformations by means of a finite number of braids, and thus give rise to universal quantum computation. The way to approximate these arbitrary unitary transformations is based on an elaborate mathematical formalism that describes the rules that the braiding and fusions of anyons must follow. For example, one of these simpler formalisms is called the Fibonacci anyon model [8]. The distinction between some non-Abelian anyons and others will be given primarily by the nature of the underlying physical system.

2.2 Topological invariants and symmetry

The study of the topological properties of matter has expanded rapidly in recent decades, due to the discovery of a wide variety of quantum many-body systems that exhibit topological phases. Examples of these kind of systems include quantum spin liquids [9], topological insulators [10], Dirac semimetals [11] and topological superconductors [12], among many others. Each of these systems shows different properties. For example,

topological insulators allow the circulation of electrons through their surface but not through their bulk, while quantum spin liquids exhibit a disorder in their spin configuration that does not disappear even at very low temperatures and show applications in quantum computing or high-temperature superconductivity.

2.2.1 The topological invariant

The topological properties of quantum matter are characterised by the type of topological invariant that characterises it. This is a quantity that is conserved under continuous deformations of the Hamiltonian, meaning that two quantum systems are topologically equivalent if their Hamiltonians can be continuously transformed into each other without changing a given property that characterises them.

As a simple example, consider the deformation between two Hamiltonians given by

$$H(\alpha) = \alpha H' + (1-\alpha)H \quad \text{with} \quad 0 \leq \alpha \leq 1, \tag{2.1}$$

and consider that we want to evaluate how its energy gap changes along this deformation. If along this continuous deformation, any of the eigenvalues of $H(\alpha)$ crosses zero, then H and H' can not topologically equivalent. Moreover, if we define the topological invariant Q as the number of energy levels above zero, and evaluate along the deformation by varying the parameter α, we can conclude that the two Hamiltonians are separated by a topological phase transition if it changes for any value of α since it is not possible to go from one to the other without closing the gap.

Topological invariants allow us to classify Hamiltonians. Once we have identified one of these invariants, we can classify all quantum Hamiltonians according to their value, and thus to account for the different topological phases they generate[13].

2.2.2 The role of symmetry

Symmetries have a profound influence on the properties of quantum systems, as well as on the type of topological invariant that they are allowed to exhibit. For example, a system composed of half-integer spins which shows time-reversal symmetry follows the Kramer's degeneracy theorem, which states that all of its energy eigenstates are doubly degenerate, because for every energy eigenstate allowed there is another eigenstate with the same energy related by time reversal.

Another, more relevant example, is the topological invariant associated with particle-hole symmetry. This symmetry, which is foundational for superconducting systems, allows for the conservation of pairs of particles. In physical systems, this allows for the creation and annihilation of Cooper pairs of electrons. For example, a Hamiltonian of the form

$$H = \sum_{nm} H_{nm} c_n^\dagger c_m + \frac{1}{2}\left(\Delta_{nm} c_n^\dagger c_m^\dagger + \Delta_{nm}^* c_m c_n\right) \tag{2.2}$$

has particle-hole symmetry, since, naively, one can see that it is invariant under the transformation $c_n \to c_n^\dagger$. A more rigorous way to prove this symmetry is to express the Hamiltonian in its Bogoliubov-de Gennes form by gathering all its fermionic operators in a vector $C = \left(c_1, \dots, c_n, c_1^\dagger, \dots, c_n^\dagger\right)^T$ so that 2.2 takes the form

$$H = \frac{1}{2} C^\dagger H_{\text{BdG}} C \quad \text{with} \quad H_{\text{BdG}} = \begin{pmatrix} H & \Delta \\ -\Delta^* & -H^* \end{pmatrix}. \tag{2.3}$$

On this new form, the Hamiltonian is symmetric under the operator $\mathscr{P} = \tau_x \mathscr{K}$ as

$$\mathscr{P} H_{\text{BdG}} \mathscr{P}^{-1} = -H_{\text{BdG}}, \tag{2.4}$$

which causes the spectrum of the system to be symmetric around zero energy. This forces that for every eigenvector ψ with energy E there exists another eigenvector $\mathscr{P}\psi$ with energy $-E$, and therefore the parity of these states is preserved.

Because this symmetry underlies the properties of superconductors, it will also apply to topological superconductors among which are the Kitaev model or parafermion chains. Therefore, we can expect these models to preserve the parity of fermions in some way. In the following chapters we will see how this parity conservation induces the appearance of edge modes, which will have applications in quantum computing due to their non-Abelian statistics.

2.3 Conformal field theory

In this section we will outline some of the characteristics of conformal field theories as they describe the properties of critical points in quantum phase transitions. In a nutshell, a conformal field theory is a field theory that is invariant under a symmetry group called the conformal group. In the case of a quantum conformal field theory, such symmetries are realised by unitary or antiunitary operators, and the theory gives rise to a unitary projective representation of the conformal group.

The study of conformal field theories is appealing for several reasons. The first of these is that CFTs allow us to rigorously formalise the definition of some quantum field theories (QFTs), which are commonly used to describe high-energy or condensed matter physical systems. Typically, quantum field theories have mass or energy scales that break the scale symmetry present in CFTs, and also act as an effective description of the underlying theory by including a cut-off parameter after regularisation. This parameter limits the energies that can occur within the QFT. However, a conformal field theory is by definition scale invariant and is not constrained by such a parameter. Another reason, and more important for this work, is that conformal field theories allow us to study the critical points of second order quantum phase transitions. These transitions, characterised by the divergence of the correlation length, embody many topological phase

transitions. Therefore, understanding them can be useful to characterise, for example, their phase transitions and different phases.

In this section we will briefly describe the fundamentals of conformal field theories, based on the well-known summaries by P. Gisparg [14] and D. Tong [15]. In the following chapters we will characterise phase transitions using the properties of the underlying conformal field theory. To do this, we will first describe what we mean by conformal field theory from a classical point of view. Then we will discuss the transition from quantum to conformal field theories by means of a procedure called radial quantization. Finally, we will study their stress-energy tensor and how it characterises these theories in terms of the central charge.

2.3.1 Classical CFT in d dimensions

In its most general form, a conformal transformation is the coordinate transformation $x \to x'(x)$ that transforms the metric of a Riemannian manifold $\mathscr{M} = \mathbb{R}^{p,q}$ defined as

$$g_{\mu\nu} = \text{diag}(1, 1, \dots, -1, -1, \dots), \tag{2.5}$$

where the signature has p positive signs and q negative signs. We say that the coordinate transformation is conformal if the manifold metric is transformed into the form

$$g_{\mu\nu}(x) \to g'_{\mu\nu}(x') = \Omega(x')g_{\mu\nu}(x') \quad \text{with} \quad \Omega(x) > 0, \tag{2.6}$$

where $\Omega(x)$ is a scale factor. This type of transformations preserve the angles between two tangent vectors u^μ and v^ν of the manifold, as the quantity

$$\angle_\theta = \frac{g_{\mu\nu}u^\mu v^\nu}{\sqrt{(g_{\mu\nu}u^\mu v^\nu)^2}} \tag{2.7}$$

is preserved under the transformation. A visual representation of a conformal transformation in two dimensions can be seen in Figure 2.2.
After this, we can define the conformal group over $\mathscr{M}$ as the connected component bound to the identity of the group formed by all the conformal transformations of the manifold $\mathscr{M}$.

We can classify the components of an arbitrary conformal transformation by considering an infinitesimal transformation given by $x^m u \to x^m u + \epsilon^\mu(x)$. Notice how ϵ is an arbitrary infinitesimal transformation dependent on x. In this case the metric transforms as

$$ds^2 \to ds^2 + \left(\partial_\mu\epsilon_\nu + \partial_\nu\epsilon_\mu\right) dx^\mu dx^\nu, \tag{2.8}$$

and it can be shown how this identity is equivalent to

$$\left(\eta_{\mu\nu}\Box + (d-2)\partial_\mu\partial_\nu\right)\partial\cdot\epsilon = 0. \tag{2.9}$$

When the dimension of the CFT is greater than 2, all the components of $(\partial\cdot\epsilon)$ higher than third order vanish, meaning that ϵ is at most quadratic in x. This allows us to classify a

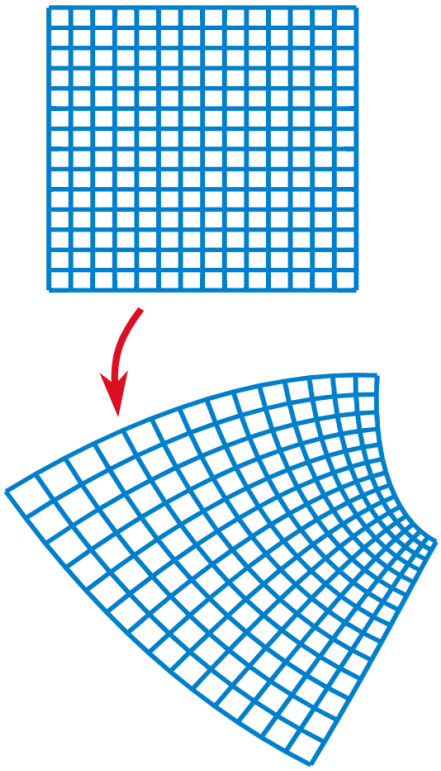

Figure 2.2: Example of a conformal transformation in two dimensions.

conformal transformation in terms of four components:

- Zeroth order in x: spacetime translations.

$$\epsilon^\mu = a^\mu$$

- First order in x: rotations and scale transformations.

$$\epsilon^\mu = \omega^\mu_\nu x^\nu$$

$$\epsilon^\mu = \lambda x^\mu$$

- Second order in x: special conformal transformations

$$\epsilon^\mu = b^\mu x^2 - 2x^\mu b \cdot x$$

We can see how the first two components constitute the symmetries of the Poincaré group present in the theory of special relativity, while the last two components impose additional symmetries upon it. In equation 2.9 we can see how the case $d = 2$ is a special case. Indeed, as we will see below, conformal field theories in two dimensions present particular properties that differentiate them from the general case.

2.3.2 Classical CFT in 2 dimensions

In two dimensions, more particularly for manifolds of the type $\mathscr{M} = \mathbb{R}^{(2,0)}$ in which $g_{\mu\nu} = \delta_{\mu\nu}$, the relation 2.8 becomes the Cauchy-Riemann equations

$$\partial_1\epsilon_1 = \partial_2\epsilon_2, \quad \partial_1\epsilon_2 = -\partial_2\epsilon_1. \tag{2.10}$$

This allows us to introduce complex coordinates in the form $z = x^1 + ix^2$ and $\overline{z} = x^1 - ix^2$ so that we can rewrite the two-component conformal transformation in a natural way as

$$\epsilon(z) = \epsilon^1 + i\epsilon^2 \qquad \overline{\epsilon}(\overline{z}) = \epsilon^1 - i\epsilon^2. \tag{2.11}$$

Thus, the conformal transformations in two dimensions are described by holomorphic functions $f(z)$, of the form

$$z \to f(z), \qquad \overline{z} \to \overline{f}(\overline{z}). \tag{2.12}$$

We can distinguish two types of conformal transformations depending on whether the associated holomorphic function $f(z)$ has a holomorphic inverse $f^{-1}(z)$ or not. The requirement that the functions $f(z)$ must also have a holomorphic inverse is very constraining, since it forces these functions to take the form

$$f(z) = \alpha z + \beta, \qquad \overline{f}(\overline{z}) = \gamma z + \delta \tag{2.13}$$

The conformal transformations specified by this class of functions receive the name of global conformal transformations, since they do not give rise to singularities at any point in the manifold $\mathscr{M}$.

On the other hand, the conformal transformations associated to holomorphic functions $f(z)$ without any additional requirements are called local conformal transformations. Because this set of functions is much broader than those given by 2.13, the theories invariant under this set of transformations are much more restricted, and we will see later how this will allows us to solve them. This distinction between global and local conformal transformation is unique to conformal field theories in 2 dimensions.

It can be shown that the generators of the infinitesimal local conformal transformations take the form

$$l_n = -z^{n+1}\partial_z \quad \bar{l}_n = -\overline{z}^{n+1}\partial_{\overline{z}}, \tag{2.14}$$

and obey an infinite-dimensional Lie algebra given by

$$[l_m, l_n] = (m-n)l_{m+n} \quad \left[\bar{l}_m, \bar{l}_n\right] = (m-n)\bar{l}_{m+n}, \tag{2.15}$$

which is called the Witt algebra.

2.3.3 Quantum CFT in 2 dimensions: radial quantization and OPE

The next step is to analyse what happens to the fields of the theory when they experience a conformal transformation. For this purpose, it is simpler to study the effects of the transformations using the Jacobian of the transformation instead of the Ω factor. Starting with the general case for d dimensions, the Jacobian of the transformation takes the form

$$\left|\frac{\partial x'}{\partial x}\right| = \Omega^{-d/2}. \tag{2.16}$$

For instance, for scale transformations we have the Jacobian $\left|\frac{\partial x'}{\partial x}\right| = \lambda^d$.

Given a theory with conformal invariance, there exist a set of ϕ_j fields which we will call "quasi-primary" which transform under global conformal transformations as:

$$\phi_j(x) \to \left|\frac{\partial x'}{\partial x}\right|^{\Delta_j/d} \phi_j(x'), \tag{2.17}$$

where Δ_j is called the scaling dimension of the field. These fields receive this name because they are covariant under the transformations, since their correlation functions satisfy

$$\langle \phi_1(x_1) \dots \phi_v(x_n) \rangle = \left|\frac{\partial x'}{\partial x}\right|_{x=x_1}^{\Delta_1/d} \dots \left|\frac{\partial x'}{\partial x}\right|_{x=x_n}^{\Delta_n/d} \left\langle \phi_1(x_1') \dots \phi_n(x_n') \right\rangle. \tag{2.18}$$

Returning to two dimensions, we can generalize this transformation to define **primary fields** as those that transform into the form

$$\Phi(z,\overline{z}) \to \left(\frac{\partial f}{\partial z}\right)^h \left(\frac{\partial \overline{f}}{\partial \overline{z}}\right)^{\overline{h}} \Phi(f(z),\overline{f}(\overline{z})). \tag{2.19}$$

The transition from a classical conformal field theory to a quantum one involves a procedure called **radial quantisation**. We will not go into the details of this procedure in this short introduction, leaving the details to the literature [15, 14]. However, its worth mentioning that it is necessary to compactify one of the two coordinates into a circle, which parametrises the CFT in a cylinder instead of in a plane. This transformation allows the use of powerful tools such as contour integrals or complex analysis when dealing with quantum conformal field theories.

The practical result of this quantization is the definition of quantum **primary operators** as those that transform in the form

$$\hat{\Phi}(z,\overline{z}) \to \left(\frac{\partial f}{\partial z}\right)^h \left(\frac{\partial \overline{f}}{\partial \overline{z}}\right)^{\overline{h}} \hat{\Phi}(f(z),\overline{f}(\overline{z})). \tag{2.20}$$

These fields are very useful since they can be used inside the so-called **operator product expansion** (OPE). It can be shown how, given two primary operators $\hat{O}_i(z,\overline{z})$ and

$\hat{O}_j(w,\overline{w})$ at points $(z,\overline{z})$ and $(w,\overline{w})$ of the manifold, we can pose the following relation:

$$\hat{O}_i(z,\overline{z})\hat{O}_j(w,\overline{w}) = \sum_k c_{ij}^k(z-w,\overline{z}-\overline{w})\hat{O}_k(w,\overline{w}). \tag{2.21}$$

This relation is called the operator product expansion and allows us to find out what happens to the operators when they approach each other in the manifold. It is important to note that this relation is purely formal and only makes sense as long as it is evaluated within correlation functions, as

$$\langle \hat{O}_i(z,\overline{z})\hat{O}_j(w,\overline{w}) \quad \bullet\rangle = \sum_k c_{ij}^k(z-w,\overline{z}-\overline{w})\langle \hat{O}_k(w,\overline{w}) \quad \bullet\rangle, \tag{2.22}$$

where $\bullet$ is a placeholder for another operator. The relevant information is in the singular part of the OPE, that is, when the operators converge to the same point in the manifold when $z \to w$ and $\overline{z} \to \overline{w}$.

2.3.4 The stress-energy tensor and the central charge

The classical stress-energy tensor is defined as the matrix of conserved currents which arises from translational symmetries $\delta x^\alpha = \epsilon^\alpha$. After radial quantization, we can obtain an analogous version to describe conformal field theories. In this case, it exhibits the properties of being symmetric and traceless $\hat{T}^\mu_\mu = 0$.

Once we have the stress-energy tensor, we can apply the operator product expansion to obtain very useful information in order to characterize the conformal field theory and its algebra. The operator product expansion between the stress-energy tensor $\hat{T}(z)$ and a primary field $\hat{\Phi}(w,\bar{w})$ is of the form

$$\hat{T}(z)\hat{\Phi}(w,\overline{w}) = \frac{h}{(z-w)^2}\hat{\Phi}(w,\overline{w}) + \frac{1}{z-w}\partial_w\hat{\Phi}(w,\overline{w}) + \dots, \tag{2.23}$$

which will be very useful to construct the Lie algebra corresponding to the conformal transformations of the stress-energy tensor.

Simultaneously, the operator product expansion of the stress-energy tensor with itself takes the form

$$\begin{aligned}
\hat{T}(z)\hat{T}(w) &= \frac{c/2}{(z-w)^4} + \frac{2}{(z-w)^2}\hat{T}(w) + \frac{1}{z-w}\partial\hat{T}(w) \\
\hat{\overline{T}}(\overline{z})\hat{\overline{T}}(w) &= \frac{\overline{c}/2}{(\overline{z}-\overline{w})^4} + \frac{2}{(\overline{z}-\overline{w})^2}\hat{\overline{T}}(w) + \frac{1}{\overline{z}-\overline{w}}\overline{\partial}\hat{\overline{T}}(w),
\end{aligned} \tag{2.24}$$

where c is called the **central charge** of the theory. A priori it might seem that c and $\overline{c}$ are independent constants. However, there is a restriction given by so-called modular invariance that forces $c = \overline{c}$.
Note how the term corresponding to the central charge prevents $\hat{T}(w)$ from being a primary field given by 2.23. Actually, it turns out that the value of c labels the conformal

group representation provided by the theory. In other words, we can uniquely characterize the CFT if we know the value of its central charge.

2.3.5 The Virasoro algebra and minimal models

We now proceed to calculate the Lie algebra corresponding to the conformal group. For this purpose, we expand the stress-energy tensor in its Laurent expansion

$$\hat{T}(z) = \sum_{n\in\mathbf{Z}} z^{-n-2} L_n, \quad \hat{\overline{T}}(\overline{z}) = \sum_{n\in\mathbf{Z}} \overline{z}^{-n-2} \overline{L}_n, \tag{2.25}$$

and invert the identities to obtain

$$\hat{L}_n = \oint \frac{dz}{2\pi i} z^{n+1} \hat{T}(z), \quad \hat{\overline{L}}_n = \oint \frac{d\overline{z}}{2\pi i} \overline{z}^{n+1} \hat{\overline{T}}(\overline{z}). \tag{2.26}$$

The commutator between the two operators yields the Lie algebra of the CFT, called the Virasoro algebra,

$$\begin{aligned}
\left[\hat{L}_n, \hat{L}_m\right] &= (n-m)\hat{L}_{n+m} + \frac{c}{12}\left(n^3 - n\right)\delta_{n+m,0}, \\
\left[\hat{\overline{L}}_n, \hat{\overline{L}}_m\right] &= (n-m)\hat{\overline{L}}_{n+m} + \frac{c}{12}\left(n^3 - n\right)\delta_{n+m,0}, \\
\left[\hat{L}_n, \hat{\overline{L}}_m\right] &= 0.
\end{aligned} \tag{2.27}$$

We can see how this algebra is an extension of the Witt algebra 2.15 found for classical conformal field theories, due to a term proportional to the central charge. For this reason, we see that in the case of $c = 0$ the conformal field theory "loses its quantum character". Also, the only element capable of giving rise to distinct algebras is precisely the central charge. Therefore, this points out that it is a key element when characterizing the CFT.

Starting from the Virasoro algebra given by 2.27, we can obtain information about the Hilbert space associated to the theory. To that end, one starts with a set of primary states defined by 2.19, and acts on them with the generators of the algebra, resulting in new states called descendants. These descendants are organized into representations of the algebra called Verma modules.

When the central charge c of the theory takes a value of

$$c = 1 - \frac{6(m' - m)^2}{mm'}, \tag{2.28}$$

where m and m' are positive and coprime, the theory is called a **minimal model** and contains only a finite number of primary fields. This simple algebraic structure allows to build the whole Hilbert space of the theory by acting with the generators of the algebra on its primary fields.

In the following table we see a set of minimal models with their corresponding central

charge.

(m, m')	Name	Central charge
(3,2)	Trivial CFT	0
(4,3)	Ising model	1/2
(5,4)	Tricritical Ising model	7/10
(6,5)	3-state Potts model	4/5
(7,6)	Tricritical 3-state Potts model	6/7

Table 2.1: Some minimal models with their corresponding central charge

We can see that models such as the Ising model or the Potts model, which will be of great interest to us later when studying parafermion chains, are minimal models. This will prove useful when trying to characterise the phase transitions of the systems using conformal information such as the scaling dimensions of the underlying theory.

2.4 The renormalization group

The **renormalization group** is the name given to a set of techniques for analysing the behaviour of critical and equilibrium quantum systems. Essentially, these techniques are based on reformulating the parameters that define a quantum system in terms of other parameters that potentially simplify it, while preserving those aspects of the problem that are of interest [16].

The renormalization group is based on the scale invariance of critical quantum systems. In particular, the critical points of second order phase transitions exhibit a divergence of the correlation length ξ, which represents the average length at which the different elements of the system are correlated to each other. This means that quantum critical points display scale invariance, which is not surprising since, as we have seen, they are described by a conformal field theory.

By performing transformations on the couplings of the system, for example in the form of coarse-graining transformations, we can replace them by other which represent the system as seen on a different scale as displayed in Figure 2.3. Then, we can study the change in the state of the system after performing a finite number of such coarse-graining transformations, which will be described by a so-called **renormalization group flow**. This flow will transport a given state of the system along a trajectory in parameter space, coming to a stop at a point that is not affected by changes in scale, i.e., critical points with scale invariance, known in this context as **fixed points**.

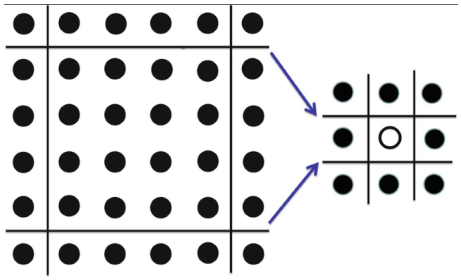

Figure 2.3: Representation of a coarse-grainig transformation in two dimensions.

2.4.1 General theory

Given a Hamiltonian and a set of couplings, represented by its parameters and condensed into a vector $\{K\}$, we can view a coarse-graining transformation $\mathscr{R}$ as a map between the couplings $\{K\} \to \{K'\} = \mathscr{R}(\{K\})$. The particular form of $\mathscr{R}$ will depend on the details of the system and on the rescaling parameter b specifying how many degrees of freedom are coarsed together, and will preserve the partition function of the system between the original Hamiltonian $H(s)$ and the coarse-grained Hamiltonian $H'(s')$:

$$Z = \mathrm{Tr}_s\, e^{-H(s)} = \mathrm{Tr}_{s'}\, e^{-H'(s')} \tag{2.29}$$

If $\mathscr{R}$ is differentiable at the fixed point K^*, we can pose the following linear equation for K' near it,

$$K'_a - K^*_a \sim \sum_b T_{ab} \left(K_b - K^*_b\right), \tag{2.30}$$

where $T_{ab} = \left.\frac{\partial K'_a}{\partial K_b}\right|_{K=K^*}$. If we denote the eigenvalues of the matrix T_{ab} as λ^i and its eigenvectors as $\{\phi^i\}$, such that

$$\sum_a \phi^i_a T_{ab} = \lambda^i \phi^i_b, \tag{2.31}$$

then we can define the **scaling variables** as linear combinations of the deviations from the fixed point $K_a - K^*_a$ as

$$u_i = \sum_a \phi^i_a \left(K_a - K^*_a\right). \tag{2.32}$$

The scaling variables transform multiplicatively near the fixed point, as

$$u'_i = \sum_a \phi^i_a \left(K'_a - K^*_a\right) = \sum_{a,b} \phi^i_a T_{ab} \left(K_b - K^*_b\right) = \sum_b \lambda^i \phi^i_b \left(K_b - K^*_b\right) = \lambda^i u_i. \tag{2.33}$$

Then, defining the **renormalization group eigenvalues** y_i implicitly as $\lambda^i = b^{y_i}$, we can distinguish the following three cases:

- If $y_i > 0$, u_i is said to be *relevant* and repeated renormalization group iterations will drive the state of the system defined by the couplings $\{K\}$ away from its fixed point value.
- If $y_i < 0$, u_i is said to be *irrelevant* and the state will iterate towards zero after repeated renormalization group iterations if it is sufficiently close to the fixed point.

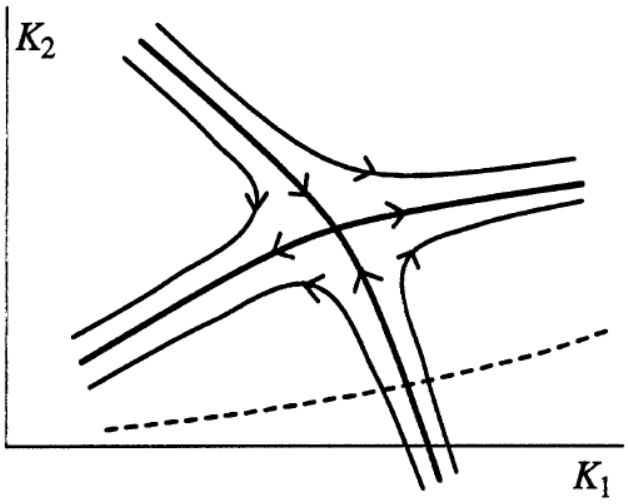

Figure 2.4: Example of a renormalization group flow in a two-dimensional system. Extracted from [16].

- If $y_i = 0$, u_i is said to be *marginal* and we cannot tell from the linearised equations whether the couplings will move away from the fixed point or towards it.

This formalism allows us to represent the phase diagram of a system in the space defined by its couplings $\{K\}$ in terms of its renormalization group flows. For example, consider a system defined by n couplings and n' relevant eigenvalues, as well as a fixed point in its space of couplings given by $\{K^*\}$. Then, there will be $(n - n')$ irrelevant eigenvalues in its vicinity, resulting in a $(n - n')$ dimensional hyper-surface in the parameter space composed of points $\{K_i\}$ that are attracted to the fixed point after coarse-graining. Near the fixed point, this surface is nothing more than the linear space generated by the irrelevant eigenvectors ϕ^i but, by continuity, we can assume that this surface exists in a finite region around it. This surface is called the **critical surface** since the long distance properties of each system corresponding to a point on this surface will be controlled by the fixed point, and their correlation length will also be infinite.

For example, a system characterized by two couplings K_1 and K_2 may be described by a renormalization group flow as seen in Figure 2.4.

We see that, because the system shows only one irrelevant eigenvalue, its critical surface becomes a critical line. In terms of quantum many-body systems, the fixed point will correspond with a critical point described by a conformal field theory, and, in the thermodynamical limit, all the points along its critical line will be described by the same theory.

2.4.2 Critical exponents

The renormalization group provides information on how the different observables scale when performing scale transformations, encapsulated in magnitudes called **critical exponents**.

Phase transitions belong to **universality classes** with respect to these critical exponents, because their value is to a large extent independent of the specifics of the system. For example, consider the Ising model in two dimensions, characterized by two couplings. The first is the reduced magnetic variable $h = \frac{H}{k_B T_c}$ and the second is the reduced thermal variable $t = \frac{T-T_c}{T_c}$. These variables have associated scaling variables near the critical point, given by u_h with eigenvalue y_h, and u_t with eigenvalue y_t respectively. In addition, since the scaling variables must vanish when $t = h = 0$, near the critical point we can take a linear approximation with respect to t and h as

$$\begin{aligned} u_t &\approx t/t_0 \\ u_h &\approx h/h_0, \end{aligned} \tag{2.34}$$

where t_0 and h_0 are two constants.
Let us consider the free energy of the system in term of the couplings,

$$f(\{K\}) \equiv -N^{-1} \ln Z. \tag{2.35}$$

It can be shown how the singular part of this energy, f_s, transforms under coarse-graining transformations as [16]:

$$f_s(\{K\}) = b^{-d} f_s(\{K'\}), \tag{2.36}$$

where the prefactor b^{-d} comes from the number of blocks N of the system which transformsas $N' = b^{-d}N$. Then, if we express this free energy in term of the scaling variables near the critical point and in terms of n iterations of the coarse-graining transformations, we have that

$$f_s(u_t, u_h) = b^{-d} f_s(b^{y_t} u_t, b^{y_h} u_h) = b^{-nd} f_s(b^{n y_t} u_t, b^{n y_h} u_h). \tag{2.37}$$

If we take a value of n such that the condition $|b^{n y_t} u_t| = u_{t0}$ is satisfied, where u_{t0} is an arbitrary constant, after a bit of algebra we can rewrite the free energy as

$$f_s(u_t, u_h) = |u_t/u_{t0}|^{d/y_t} f_s\left(\pm u_{t0}, u_h |u_t/u_{t0}|^{-y_h/y_t}\right). \tag{2.38}$$

Finally, if we rewrite this expression in terms of the original reduced variables t and h, and if we absorb the constant u_{t_0} in t_0, we can express the free energy as a function of a **scaling function** Φ as

$$f_s(t, h) = |t/t_0|^{d/y_t} \Phi\left(\frac{h/h_0}{|t/t_0|^{y_h/y_t}}\right). \tag{2.39}$$

This scaling function is universal in the sense that it depends only on the scaling factors t_0 and h_0 defined in 2.34. We see how it does not have a strong dependence on the microscopic details of the system, which is a reflection of the universality present in the phase transitions. For example, the phase transition shown by the Ising model between the paramagnetic and ferromagnetic phase belongs to the same universality class as the

liquid-gas phase transition present in a fluid, such as water.
From this expression for the free energy and its derivatives we can express the critical exponents as a function of the renormalization group eigenvalues as follows:

- Specific heat: $C = \left.\frac{\partial^2 f}{\partial t^2}\right|_{h=0} \sim |t|^{-\alpha}$. Solving in equation 2.39, we have that $C \sim |t|^{d/y_t - 2}$. Thus,

$$\alpha = 2 - \frac{d}{y_t}. \tag{2.40}$$

- Spontaneous magnetization: $M = \left.\frac{\partial f}{\partial h}\right|_{h=0} \sim (-t)^{\beta}$. Thus,

$$\beta = \frac{d - y_h}{y_t}. \tag{2.41}$$

- Magnetic susceptibility $\chi = \left.\frac{\partial M}{\partial H}\right|_{H=0} \sim |t|^{-\gamma}$. Thus,

$$\gamma = \frac{2y_h - d}{y_t} \tag{2.42}$$

- Magnetization at $T = T_c$: $M = \left.\frac{\partial f}{\partial h}\right|_{T=T_c} \sim |h|^{1/\delta}$.Thus, Therefore,

$$\delta = \frac{y_h}{d - y_h}. \tag{2.43}$$

We see how the four main thermodynamic exponents are expressed in terms of the renormalization group eigenvalues y_t and y_h. This redundancy implies that there are **scaling relations** between them, such as $\alpha + 2\beta + \gamma = 2$ or $\alpha + \beta(1 + \delta) = 2$, which precede the development of the renormalization group.
Analogously, consider a correlation function of the form

$$G(r_1 - r_2, \mathscr{H}) \equiv \langle s(r_1)\, s(r_2)\rangle_{\mathscr{H}} - \langle s(r_1)\rangle_{\mathscr{H}} \langle s(r_2)\rangle_{\mathscr{H}}\,, \tag{2.44}$$

where we can set $r \equiv r_1 - r_2$ and $h = 0$ so that the Hamiltonian is unambiguously characterized by the variable t. Then, it can be shown that it can be expressed in terms of a scaling function Ψ as

$$G(r, t) = |t/t_0|^{2(d-y_h)/y_t}\, \Psi\left(r/\,|t/t_0|^{-1/y_t}\right). \tag{2.45}$$

In this case, we can express the two remaining critical exponents as:

- Correlation length: $\xi \propto |t|^{-\nu}$, where we know that G decays as $e^{-r/\xi}$. Thus,

$$\nu = \frac{1}{y_t} \tag{2.46}$$

- Correlation function $G(r) \propto 1/r^{d-2+\eta}$. Thus,

$$\eta = 2 - (2y_h - d). \tag{2.47}$$

This allows us to develop an additional set of scaling relations, such as $\gamma = \nu(2 - \eta)$.

2.4.3 The c-theorem

It is possible to combine the concepts seen in conformal field theory and the renormalization group through a theorem called the **c-theorem** [17]. This theorem states that, given a theory represented by the space spanned by its couplings, and given two fixed points in that space at which the central charge takes some given values, the variation of the central charge through the renormalization group flow between the two points decreases monotonically.

In other words, this theorem states that the evolution of the central charge between the values of two fixed points will be a monotonic and smooth function as long as they are connected by a renormalisation group flow and this flow does not pass through any other intermediate fixed point.

Later, when characterising the phase diagram of quantum systems such as the parafermion chain, this theorem will come in handy, since we will be able to determine the value of the central charge at a fixed point and we will be able to guess that the renormalization group flow does not pass through any intermediate fixed point. This will allow us to suggest that its value remains constant throughout the flow.

2.5 Finite-size scaling

The fact that physical or numerically described systems usually have a finite dimension, given by a scale parameter L, introduces a distortion in the values of the various observables under scale transformations.

In general, given an arbitrary observable A dependent on a parameter ρ which presents a phase transition at the critical point $\rho = \rho_c$ characterized by a divergence of the correlation length ξ, it will show a scaling proportional to $|rho - \rho_c|^{-\zeta}$ in terms of a critical exponent ζ. This behaviour should hold for systems of finite size L and at scales much larger than those of the correlation length ξ. Since the correlation length diverges as $\xi \sim |\rho - \rho_c|^{-\nu}$, for $L \gg \xi$, we have that

$$A_L(\rho) \sim |\rho - \rho_c|^{-\eta} \sim \xi^{\zeta/\nu}. \tag{2.48}$$

On the other hand, for $L \ll \xi$, the size of the system L plays the role of a cut-off so that

$$A_L(\rho) \sim L^{\zeta/\nu}. \tag{2.49}$$

These considerations allow us to propose a **finite-size scaling ansatz** as

$$A_L(\rho) = L^{\zeta/\nu} \tilde{f}\left(L^{1/\nu}|\rho - \rho_c|\right), \tag{2.50}$$

where $f(x)$ is a dimensionless **scaling function** that takes a constant value for $x \to 0$, that is, when $\rho \to \rho_c$.

2.5.1 The intersection method

This ansatz allows us to calculate the critical exponents by means of the **intersection method**. At the critical point, when the observable ρ takes the value ρ_c we have that:

$$A_L(\rho_c) = L^{\zeta/\nu} \tilde{f}\,(0) = C \cdot L^{\zeta/\nu}. \tag{2.51}$$

Taking logarithms on both sides, we have that

$$\log A_L(\rho_c) = \frac{\zeta}{\nu} \log L + \log C, \tag{2.52}$$

from which we can perform a linear fit of $\log A_L(\rho_c)$ against $\log L$ to obtain the critical exponent ζ. This method receives its name from the fact that when plotting the curve for $A_L(\rho)$ given by the ansatz 2.50 for different values of ρ and L with the correct critical exponent ζ, the observable $A_L(\rho_c)$ becomes independent of the size of the system and thus one can see how the different curves intersect at the same point $\rho = \rho_c$.

This is the method that will be used to numerically compute the critical exponents of the different quantum models, once the different observables $A_L(\rho)$ are obtained using DMRG.

3 | Numerical methods

In many cases it is not possible to approach a strongly correlated quantum system analytically, because most of the techniques are available for free or weakly interacting systems. In these situations, the only option is to use numerical methods. There is a wide variety of methods applicable to strongly correlated systems, but we will focus on only two of them.

The first is the exact diagonalization of the Hamiltonian, giving place to the whole spectrum of the system and effectively solving it. The second is the variational optimization of tensor network ansätzen, which only yields a reduced set of states close to the ground state but which is computationally much more tractable. On particular, we will focus on an ansatz called the matrix product state (MPS) and a corresponding variational algorithm called the density matrix renormalization group (DMRG). We will also introduce a second ansatz called the multi-scale entanglement renormalization ansatz (MERA) because we will see how it is useful at critical points.

3.1 Exact diagonalization

Exact diagonalization (ED) is a straightforward algorithm. It is based on representing the Hamiltonian of the system numerically as a square matrix and then diagonalizing it to obtain its eigenvalues (energies) and eigenvectors (excited states).

The number of basis states in the Hilbert space $\mathscr{H}$ of the system grows exponentially with the number of elements, so diagonalization of the Hamiltonian is only possible for reasonably small systems. For example, for a one-dimensional chain of n spins, the number of basis states in $\mathscr{H}$ grows as 2^n so the total Hamiltonian grows as 2^{2n}. This makes it only reasonable to run the exact diagonalization for, at most, a few dozens of spins. To this date, the state of the art in ED for spin $\frac{1}{2}$ chains grows to about 60 spins [18].

Typically, an efficient implementation of exact diagonalization employs algorithms that exploit the symmetries of the Hamiltonian to speed up the process, such as the Lanczos algorithm. This is done because the Hamiltonian is usually very sparse (with approximately $\mathcal{O}(n)$ elements instead of the full n^2).

The advantages of exact diagonalization are, on the one hand, that it allows us to access the full spectrum of the system, and that it presents a constant computational complexity regardless of the intensity of the interactions or the criticality of the system, unlike other

methods where the computational time will depend on the complexity of the underlying phase. The disadvantages are that as we have seen we cannot study systems with a large number of components, even less in the thermodynamic limit.

3.2 Tensor networks

An entire class of numerical methods is based on the representation of the quantum state in a form that contains a smaller number of parameters. This approximation will be given by the contraction of a network of tensors. As we will see, this makes it possible to store an exponentially smaller number of parameters and thus significantly reduce the computational complexity of the algorithm. The challenge then becomes to optimize this network of tensors so that it resembles as closely as possible the original state by sequentially applying a variational algorithm.

Suppose the wave function coming from a one-dimensional system with d local basis states and d^n total basis states. Its Hilbert space takes the form $\mathscr{H} = \mathscr{H}_1 \otimes \mathscr{H}_2 \otimes \cdots \otimes \mathscr{H}_n$ and the wave function is representable as

$$|\Psi\rangle = \sum_{j=0}^{d^n} \psi_j |j\rangle = \sum_{i_1 i_2 \ldots i_n} \psi_{i_1 i_2 \ldots i_n} |i_1 \otimes i_2 \otimes \cdots \otimes i_n\rangle , \tag{3.1}$$

where i_n takes d possible values. So, the coefficients $\psi_{i_1 i_2 \ldots i_n}$ can be seen as a tensor of n indices and d^n elements.

It is possible to factor this big tensor as the contraction of a collection of smaller tensors. These tensors will have a set of "real" indices, corresponding to the indices $\{i_1 i_2 \ldots i_n\}$ of the original tensor, and a set of "auxiliary" indices corresponding to the contractions of the tensors with each other.

The main idea behind **tensor networks** is to truncate the dimension of the contracted auxiliary indices between the tensors to a value χ known as the **bond dimension**, low enough to yield an efficient representation of the wave function. Ideally, this representation captures the most relevant phenomena of the strongly correlated system to be studied, while storing a number of elements *much* smaller than the d^n of the original representation. Each of the tensor representations of the wave function is called a tensor network *ansatz*, and depending on its structure it will capture some aspects of the original wave function better than others.

Normally, to better visualize the ansatz used and to perform calculations, a pictorial notation proposed by Roger Penrose in 1971 [19] is used. Using this notation, each of the tensors is represented by a geometric shape and each of the indices is represented by external legs. In this way, the contraction of two tensors can be visualized pictorially as the contraction of their legs, and the resulting tensor structure can be evaluated more easily as can be seen in Figure 3.1.
It is important to note that, computationally, the tensor network is initialized very dif-

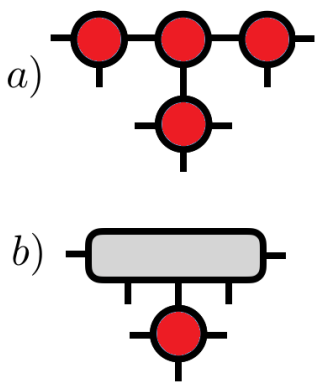

Figure 3.1: (a) Example of a 7-index tensor using Penrose notation. (b) Example of the contraction of the three top tensors returning an equivalent tensor.

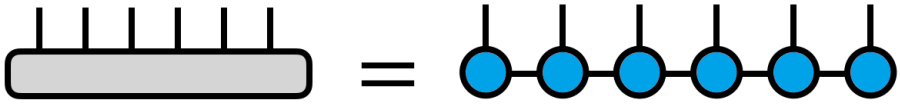

Figure 3.2: Example of a matrix product state.

ferently from the wave function it is intended to represent (for example, it can be initialized with constant or random elements). Once initialized, the challenge is to optimize the tensor network so that it resembles as closely as possible the desired wave function. Because we are trying to optimize the tensor network, the corresponding algorithms are referred as variational.

3.2.1 The matrix product state

A widely used ansatz for one-dimensional systems is known as a **matrix product state** (MPS). In it, the original tensor is decomposed into a sequence of 3-index tensors (of 2-index at the ends due to the open boundary conditions) as shown in Figure 3.2. If we set the different indexes $\{i_1 i_2 \dots i_n\}$ to a particular value, for example to represent the coefficients of the ground state, this decomposition becomes a product of matrices of dimension χ^2, with vectors of dimension χ at the ends.

Entanglement entropy and area law

Intuitively, we can understand the value of the bond dimension χ as the amount of information stored in the ansatz corresponding to the correlations between the different elements of the system. For example, if a given state described by (3.1) has no correlations between its various elements, we can understand it as simply one of the basis vectors, and therefore all the coefficients $\psi_{i_1 i_2 \dots i_n}$ are zero except one, call it $\psi^* = \psi_{i_1^* i_2^* \dots i_n^*}$. This state would be described by a single ψ^* number instead of the d^n numbers of an arbitrary state, and thus would be fully represented by the MPS taking $\chi = 1$. At the other extreme, the most strongly correlated state available would be described by a combination of all the vectors in the basis with identical coefficients, and thus would require

all d^n elements to describe it correctly. This means that the MPS would require the maximum value of χ to capture all the correlations.

The "amount of correlation" exhibited by a state is described by its **entanglement entropy**, which for the state in its density matrix form $\hat{\rho}_A$ is given by

$$S_A = -\mathrm{Tr}\hat{\rho}_A \log \hat{\rho}_A. \tag{3.2}$$

It depends on the number of elements in the system, call it L. For a system $\mathscr{H}$ with D spatial dimensions, the literature states [20] that an arbitrary state has an entanglement entropy of the form

$$S_A(L) \sim L^D, \tag{3.3}$$

while the ground state and the first excited states' entanglement entropy follows an **area law** of the form

$$S_A(L) \sim L^{D-1}. \tag{3.4}$$

Therefore, for $D = 1$ we have that the entanglement entropy of the ground state and the first excited ones obeys $S_A(L) \sim L^0$ and remains a constant. This implies that, in one spatial dimension, an efficient representation (with fairly small χ) as an MPS of the ground state and first few excited states is possible for arbitrarily large L. In practice this allows for an efficient representation of the state with L in the range of a few hundred sites.

When the ground state is critical, it can be shown that there is a **logarithmic correction** of the form

$$S_A(L) \sim \log L, \tag{3.5}$$

and therefore it is necessary to set a value of the bond dimension χ that increases with the size of the system, albeit slowly. This makes the MPS ansatz not *ideal* for systems at criticality.

3.3 The density matrix renormalization group

Once an MPS decomposition is set up, it is necessary to optimize it through a variational algorithm. The most commonly used for this is the so-called **density-matrix renormalization group** (DMRG).

It is also possible to decompose operators in an analogous way to an MPS as we can see in Figure 3.3. This is known as **matrix product operator** (MPO), and is a fundamental step in order to carry out the variational algorithm. If we decompose both the state into a MPS and the Hamiltonian of the system into a MPO, it is possible to perform an iterative procedure known as *sweeping* to minimize, one by one, the energies of each of the tensors that compose the MPS [20].

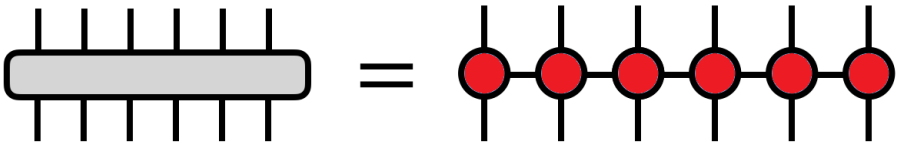

Figure 3.3: Example of a matrix product operator.

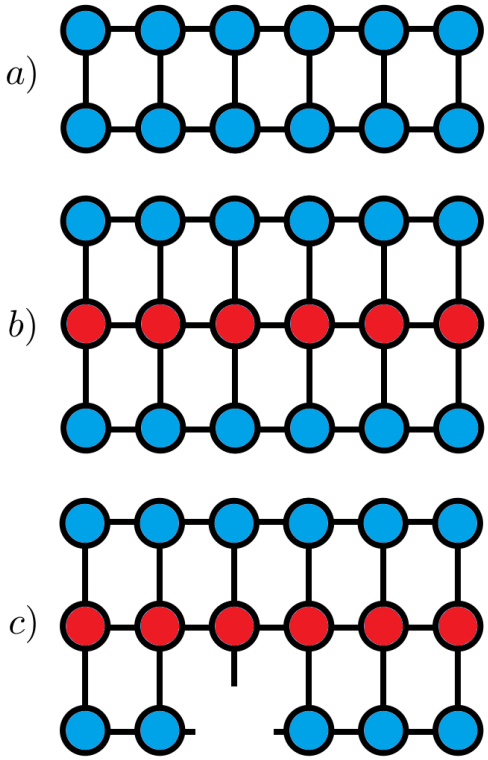

Figure 3.4: (a) Norm of the MPS state $\langle\Psi|\Psi\rangle$. b) Expected value of the energy for a given MPS and Hamiltonian, $\langle\Psi|\,H\,|\Psi\rangle$. (c) derivative $\frac{\partial}{\partial T_3^\dagger}\langle\Psi|\,H\,|\Psi\rangle$

The DMRG algorithm consists of establishing the following Lagrange multiplier problem for each of the T_i tensors that compose the MPS:

$$\frac{\partial}{\partial T_i^\dagger}[\langle\Psi| H |\Psi\rangle - \lambda \langle\Psi|\Psi\rangle] = 0, \tag{3.6}$$

where $\langle\Psi| H |\Psi\rangle$ corresponds to the contraction of the MPO with two MPS, one on each side as seen in Figure 3.4 a) and $\langle\Psi|\Psi\rangle$ refers to the contraction of the two MPS with themselves as seen in Figure 3.4 b). It can be shown how this problem can be reduced to an ordinary eigenvalue problem if we impose a certain structure on the MPS (called a mixed-canonical form with respect to T_i), and reshape T_i to a vector. The problem then becomes

$$A\vec{T_i} = \lambda\vec{T_i}, \quad \text{where} \quad A = \frac{\partial}{\partial T_i^\dagger} \langle\Psi| H |\Psi\rangle, \tag{3.7}$$

where we can identify A with the tensor at Figure 3.4 c) after reshaping it to a matrix. Once we solve this eigenvalue problem and find the value of T_i, we can substitute it into the MPS and move on to the next tensor T_{i+1} until we reach the last tensor of the MPS and finish a sweep. A complete DMRG algorithm can involve from a few sweeps for simple systems to several hundreds for complicated and/or critical systems. This variational optimization runs with a time complexity of $\mathcal{O}(\chi^3)$.

For this work, we will use the implementations of both ED and DMRG found in the Python library known as **TeNPy** [21]. It offers a robust, optimized and well-tested set of implementations for algorithms such as ED or DMRG; as well as the default implementation of a couple of strongly-correlated systems and a colletion of useful methods such as the calculation of entanglement entropies or two-point correlation functions.

3.3.1 Numerical approach

In the following we will show how we can use DMRG to extract information about the relevant quantum systems. As we have seen, DMRG allows us to optimize an *ansatz* considered on the ground state of the system by means of a variational algorithm, so that it is as close as possible to the true ground state. Once the algorithm has been completed and all sweeps have been run, we can calculate a wide variety of observables from this ansatz.

Entanglement entropy and central charge

The first of these quantities is the entanglement entropy. Given by 3.2, the entanglement entropy tells us how entangled is the state. In our particular case, we were able to extract this magnitude directly from the optimized ansatz using the TeNPy library. This magnitude is very useful since it can be fitted to the **Calabrese-Cardy formula** [22]

$$S(L, l) = S_0 + \frac{c}{6} \log\left[\frac{L}{\pi} \sin\left(\frac{\pi l}{L}\right)\right], \tag{3.8}$$

and allows us to compute the **central charge** c of the theory. This way of computing it requires the value of the entanglement entropy for a single value of L. On the other hand, inverting this formula by making $l = \frac{L}{2}$, we arrive at the relation

$$c = 6\frac{S(L, L/2) - S\left(L_{\max}, L_{\max}/2\right)}{\log\left(L/L_{\max}\right)}. \tag{3.9}$$

This allows us to compute the central charge numerically, provided we have the entanglement entropy data for two different values of L. The former way is computationally cheaper but also more imprecise, and is used for applications where it is not necessary to know precisely the exact value of the central charge, but only its relative changes; while the latter way is considerably more expensive because it needs two runs of DMRG but makes possible to obtain more accurate values of c.

Energy gaps and critical exponent z

The second quantity that we can extract using DMRG is the **energy spectrum** of the model. Once we have the optimized ansatz, it is straightforward to find its energy, and in our case, we do this by using methods from the TeNPy library [21].

We have seen how the ansatz can be optimised with respect to the ground state. However, it is also possible to optimise the ansatz with respect to excited states. This can be done by computing the different states sequentially and each time imposing an orthogonality condition on all the previously calculated states. This allows us to calculate the first few values of the spectrum of the system and from there to extract the different energy gaps. An important detail is that DMRG is only able to optimise an ansatz within the symmetry sector of the Hamiltonian in which it is initialised, and cannot go outside this sector. For this reason, it is necessary to take care when initialising the ansatz to determine the desired sector.

After these considerations, we are able to compute the first energy levels of the spectrum, as well as the gaps. Then, by means of the finite-size scaling ansatz 2.50 and the intersection method, we can extract the critical exponent z of the system. In particular, it is known that the energy gap follows a scaling relation of the form [1, 23]

$$\Delta(L) = L^{-z}\bar{\Delta}\left(L^{1/\nu}\left|f - f_c\right|\right), \tag{3.10}$$

in terms of a critical exponent z and a given parameter f. This means that, when the system is in its critical point and $f = f_c$, the energy gap scales as a power law as $\Delta(L) \propto L^{-z}$. By performing a linear fit on its logarithms it is possible to calculate the value of z.

Structure factor and critical exponent η

The third quantity that we can calculate generically for any spin chain is the **structure factor**. This factor is given by the sum of all two-point correlation functions for two

operators,

$$S(L) = \sum_{i,j} \left\langle \sigma_i \sigma_j^\dagger \right\rangle. \tag{3.11}$$

From the optimised ansatz we can calculate its value, in our case using methods available in TeNPy. Finally, according to the finite-size scaling ansatz 2.50 we know that in criticality this quantity scales according to an exponent η [1] as

$$S(L) \propto L^{2-\eta}, \tag{3.12}$$

so following a method analogous to how the exponent z is calculated in 3.10 we can extract the value of η.

Callan-Symanzik β and critical exponent ν

The fourth and final quantity that we can sometimes calculate is the so-called **Callan-Symanzik β function** [24] and will only be considered when dealing with parafermion chains. It has the form

$$\beta = \frac{\Delta}{\Delta - 2\frac{\partial \Delta}{\partial \ln f}}, \tag{3.13}$$

where Δ is the energy gap and f is a parameter shown by parafermion chains. It shows a scaling behaviour as a function of a critical exponent ν [1] as

$$\beta \propto L^{-1/\nu}, \tag{3.14}$$

from which we can extract the last critical exponent $1/\nu$.

3.4 The multi-scale entanglement renormalization ansatz

The **multi-scale entanglement renormalization ansatz** (MERA) is another type of ansatz proposed to decompose the original tensor 3.1. In this ansatz, a new type of auxiliary tensor, called a disentangler, is introduced to reduce the amount of short-range entanglement between two adjacent tensors in the lower layer. This approach also considers the contraction of tensor layers in an additional dimension, leading to a layered structure. This allows for a much better extraction of quantum information at critical points, and can be shown how it works in an analogous way to the coarse-graining transformations seen for the renormalisation group in the previous section. It is known that the MERA in one dimension can capture the logarithmic correction given by the expression (3.5)[25] and is therefore the natural choice for studying systems in criticality.

Once a MERA has been numerically initialised, it must be optimised using a variational procedure. The procedure is analogous to that used in DMRG, but much more complex. We refer the interested reader to the specific details of the implementation available in [26]. However, it is relevant to note that the time complexity of its variational optimisation runs as $\mathcal{O}(\chi^7)$, as opposed to the $\mathcal{O}(\chi^3)$ complexity of DMRG, which in practice avoids the use of bond dimensions larger than about 20 to 30. This is contrary to the

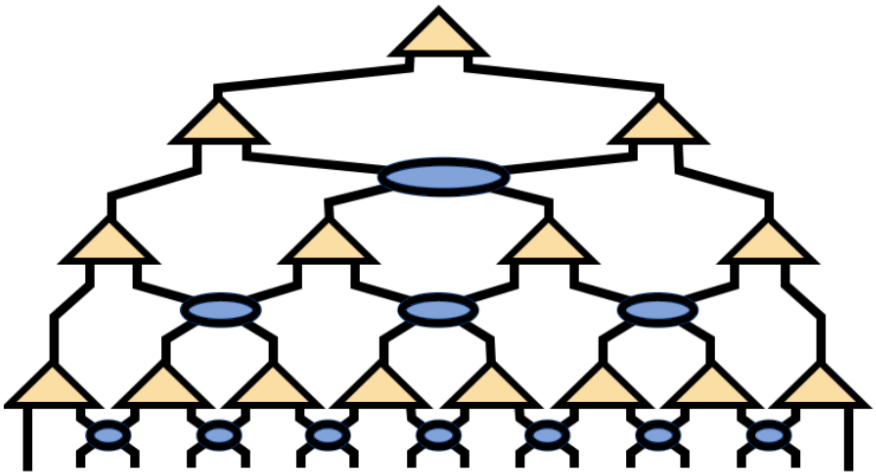

Figure 3.5: Example of a binary MERA. The disentanglers are shown as yellow triangles while the tensors are shown as blue ellipses.

values in the order of several hundreds that can be easily achieved by DMRG.

The advantage of this approach is that once the optimised MERA is obtained, it is possible to extract information about the underlying CFT. For example, there is an algorithm that is able to extract the scaling dimensions of the CFT as well as all the information about the scaling operators of the theory [27]. This information can, in turn, be used to classify the type of conformal field theory that underlies a given phase transition.

For this work we will use a MERA algorithm that is directly adapted from G. Evenbly's implementation in [26]. Here the author implements a modified binary MERA algorithm, as well as the corresponding conformal data extraction algorithms. We will adapt it by simply providing it with the corresponding Hamiltonians we are interested in, and incorporating the outputs into the rest of the code to process the results.

4 | The Kitaev model

One of the first strongly correlated models known to have a topological phase is the Kitaev model. Discovered by the Russian physicist Alexei Kitaev in 2001 [28], this toy model has edge modes in its topological phase, called Majorana edge modes, which are non-Abelian anyons due to their exchange statistics. These non-Abelian anyons induce a transformation of the quantum state of the system when they are spatially exchanged, leading to potential applications.

In this section we will study some of the basic features of the Kitaev model, as well as its formulation in terms of spins via the Jordan-Wigner transformation, leading to the quantum Ising model. We will study the analytical solution of the quantum Ising model, as well as its phase transition separating the topological and trivial phases, characterised by an underlying free-fermion conformal field theory. Next, we will explore in more detail the applications of Majorana zero modes to quantum computation, as well as the problems of achieving universality. Finally, we will conclude the section by incorporating an interaction term into the quantum Ising model to arrive at the axial-nearest-neighbour Ising model (ANNNI model), which will later be of considerable interest when analysing parafermion chains.

Since the quantum Ising model, and hence the equivalent Kitaev model, is one of the few strongly correlated models that can be solved analytically, it is an excellent benchmark for testing analytical and numerical techniques before applying them to other systems.

4.1 Introduction

The **Kitaev model** is a one-dimensional quantum system consisting of a chain of n spinless fermions interacting with their nearest neighbours via three different terms. Using open boundary conditions, it is described by the Hamiltonian

$$H = \sum_{i=1}^{n-1} \left(-t \cdot c_i^\dagger c_{i+1} + \Delta \cdot c_i c_{i+1} \right) - \sum_{i=1}^{n} \left(\mu \cdot c_i^\dagger c_i + \frac{1}{2} \right) + \text{H.c.}, \tag{4.1}$$

where the term t corresponds to a fermion exchange interaction (hopping term), the term Δ corresponds to the formation and destruction of fermion pairs (superconducting term) and the term μ is a chemical potential acting on the number of fermions $\mathcal{N} = c_i^\dagger c_i$ as represented in Figure 4.1. The term H.c. indicates the addition of the complex conjugates

of each operator, so that the Hamiltonian is hermitian. This model shows a topological phase with corresponding edge modes due to the particle-hole symmetry of the Hamiltonian. This symmetry can be rigorously checked by expressing the Hamiltonian in its Bogoliubov-de Gennes form as was shown in 2.4.

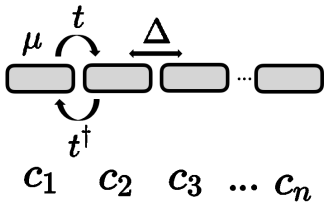

Figure 4.1: Schematic representation of the Kitaev model.

4.1.1 Majorana zero modes

This system, when it is in the topological phase, yields two edge modes called **Majorana zero modes**. They receive this name because they have zero energy and zero charge, and they represent their own antiparticle in the same way as the theoretical particle hypothesized by Ettore Majorana in 1937 [29].

To show the presence of the zero modes, let us introduce a combination of two Majorana operators a_i, b_i,

$$c_i = \frac{1}{2}\left(a_i + ib_i\right), \quad c_i^\dagger = \frac{1}{2}\left(a_i - ib_i\right) \tag{4.2}$$

which satisfy the following algebra

$$\begin{aligned} &a_i^\dagger = a_i \quad b_i^\dagger = b_i \\ &\left\{a_i, a_j\right\} = \left\{b_i, b_j\right\} = 2\delta_{ij} \\ &\left\{a_i, b_j\right\} = 0. \end{aligned} \tag{4.3}$$

Note that it imposes $a_i^\dagger = a_i$, so the particle is by definition its own antiparticle. We can simplify the system without loss of generality by making $t = \Delta$ to get the Hamiltonian

$$H = it \sum_{i=1}^{n-1} b_i a_{i+1} - \frac{i}{2}\mu \sum_{i=1}^{n} a_i b_i, \tag{4.4}$$

from which we can look at two limiting cases. First, if $t = 0$ and $\mu < 0$, the Majorana Hamiltonian (4.4) becomes

$$H = -\frac{i}{2}\mu \sum_{i=1}^{n} a_i b_i, \tag{4.5}$$

which is a topologically trivial state where each site is populated by pairings of Majo-

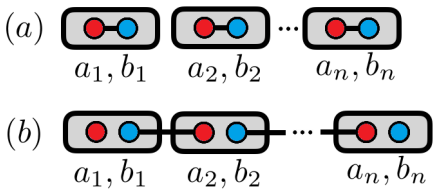

Figure 4.2: Schematic illustration of the two limiting cases of Hamiltonian (4.4). (a) Trivial phase when $t = 0$ as seen in case (4.6). (b) Topological phase when $\mu = 0$ as seen in case (4.7) with unpaired Majoranas at the ends of the chain.

ranas $a_i b_i$, as seen in Figure 4.2 (a). However, when $\mu = 0$ the Hamiltonian becomes

$$H = it \sum_{i=1}^{n-1} b_i a_{i+1}, \tag{4.6}$$

and at $i = 0$ and $i = n-1$ we find unpaired operators at the edges (a_1 and b_n respectively) as seen in Figure 4.2 (b). It can be shown that these operators commute with the Hamiltonian, so they are conserved quantities and they possess zero energy.

We can reformulate this Hamiltonian once again in terms of fermions defined as $d_i = \frac{1}{2}(a_{i+1} + ib_i)$. Replacing them, the Hamiltonian takes the form

$$H = -\frac{t}{2} \sum_{i=1}^{n-1} \left(d_i^\dagger d_i - \frac{1}{2} \right). \tag{4.7}$$

In this alternative formulation, the unpaired a_1 and b_n operators sitting at the edges of the chain yield two fermions $f = \frac{1}{2}(a_1 + ib_n)$ and $f^\dagger = \frac{1}{2}(a_1 - ib_n)$. This fermions are highly non-local because they This fermions still commute with the Hamiltonian, meaning that they also possess zero energy and the ground state is doubly degenerate.

The degeneracy of the Hamiltonian, usually seen as the closing of the energy gap, is a clear indication of the existence of a topological phase and the emergence of edge modes. It will show up in subsequent generalizations of the Kitaev model that we will consider in the following chapters.

4.2 The Jordan-Wigner transformation

We can learn more about these phases by looking at the spin chain representation of the Kitaev model. This is done via the **Jordan Wigner transformation**, which maps the fermionic operators c_i to spin operators given by the Pauli operators σ_x and σ_z. It is given by

$$\begin{aligned} \sigma_i^z &= 1 - 2c_i^\dagger c_i \\ \sigma_i^x &= \prod_{j<i} \left(1 - 2c_j^\dagger c_j\right) \left(c_i + c_i^\dagger\right), \end{aligned} \tag{4.8}$$

and is highly non local, in the sense that it maps well-localized operators at site i to strings of operators along all the chain $j < i$ called Jordan-Wigner strings. The spin degrees of freedom are 'unphysical' from the point of view of the fermions because they are not measurable locally, so this can be seen as a very useful but purely mathematical trick.

The resulting chain is known as the **quantum Ising model**,

$$H = -t \sum_{i=1}^{n} \left(\sigma_i^x \sigma_{i+1}^x - \frac{\mu}{2t} \sigma_i^z \right), \tag{4.9}$$

which is known to have a paramagnetic phase for $\left|\frac{\mu}{2t}\right| > 1$ and a ferromagnetic phase for $\left|\frac{\mu}{2t}\right| < 1$ with a quantum phase transition in between them.

In the paramagnetic (disordered) phase, the spins do not prefer to align in a particular direction. The corresponding phase in the fermion picture is a topologically trivial band insulator with a finite energy gap. On the other hand, in the ferromagnetic (ordered) phase, the spins tend to align in the direction of σ^z and the corresponding fermionic phase is topological with a closing of the energy gap due to the double degeneration of the ground state.

However, these two situations do not correspond to the extreme cases where t was set to 0 as in 4.6. Moreover, we do no longer find that the unpaired a_1 and b_n operators commute with the Hamiltonian as in 4.7 so we have to be a little more precise about how we analyse the phases. The way forward is to postulate an *ansatz* for the Majorana operators as

$$\Psi_{\text{left}} = \sum_{i=1}^{n} \left(-\frac{\mu}{2t} \right)^{i-1} a_i, \qquad \Psi_{\text{right}} = \sum_{i=1}^{n-1} \left(-\frac{\mu}{2t} \right)^{i} b_{n-i} \tag{4.10}$$

These ansätze, which can be shown to correspond to the Majorana states, do not commute exactly with the Hamiltonian but do tend to zero exponentially, as

$$[H, \Psi_{\text{left}}] = i\mu \left(-\frac{\mu}{2t} \right)^{n-1} b_n \qquad \left[H, \Psi_{\text{right}}\right] = i\mu \left(-\frac{\mu}{2t} \right)^{n-1} a_1. \tag{4.11}$$

This is represented in Figure 4.3, and means that the gap still closes at the thermodynamic limit and therefore that we have a case similar to that of $\mu = 0$: the appearance of two zero modes without energy and a degeneracy of the ground state.

4.3 Analytical solution

The quantum Ising model (and by duality, the Kitaev model) is one of the few models of its kind that can be analytically solved by means of a **Bogoliubov transformation**. While this solution was first derived in 1961 by Lieb, Schultz and Mattis [30], we will

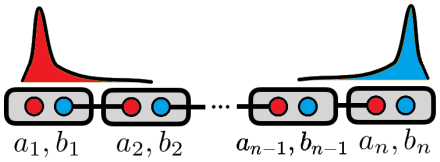

Figure 4.3: Schematic illustration of the exponential decay of Majorana zero modes.

briefly show how this is done by following the work by Calabrese et al. [31]. Here, Calabrese computed the dispersion relation for the quantum Ising model 4.9 given a number of fermions on the chain and using either periodic or anti-periodic boundary conditions depending on the parity of this number. While this is done to simplify the calculation, there also exists an analytical procedure for open boundary conditions as found in [32].

For an even number of fermions in the chain, after imposing anti-periodic boundary conditions the dispersion relation takes the form

$$\epsilon_{k_n} = 2 - t\sqrt{1 + h^2 - 2h\cos(k_n)}, \tag{4.12}$$

where $h \equiv -\left|\frac{\mu}{2t}\right|$ and L is the length of the chain. The momenta k_n allowed for the fermions is quantized in the anti-periodic sector as

$$k_n = \frac{2\pi(n + 1/2)}{L}, \quad n = -\frac{L}{2}, \ldots \frac{L}{2} - 1, \tag{4.13}$$

and the Hamiltonian takes the diagonal form

$$H_e(h) = \sum_{n=-\frac{L}{2}}^{\frac{L}{2}-1} \epsilon(k_n)\left[\alpha_{k_n}^\dagger \alpha_{k_n} - \frac{1}{2}\right]. \tag{4.14}$$

On the other hand, for an odd number of fermions and after imposing periodic boundary conditions we can express the Hamiltonian in an analogous way but incorporating an additional term, as

$$H_o(h) = \sum_{\substack{n=-\frac{1}{2} \\ n\neq 0}}^{\frac{L}{2}-1} \epsilon(p_n)\left[\alpha_{p_n}^\dagger \alpha_{p_n} - \frac{1}{2}\right] - 2t(1-h)\left[\alpha_0^\dagger \alpha_0 - \frac{1}{2}\right]. \tag{4.15}$$

On this occasion, the moments are quantized in the periodic sector as

$$p_n = \frac{2\pi n}{L}, \quad n = -\frac{L}{2}, \ldots \frac{L}{2} - 1. \tag{4.16}$$

By combining both results and ordering the energy levels for all allowed quantized momenta k_n and p_n, for all possible numbers of fermions n, we can analytically compute the energy levels of the quantum Ising model spectrum.

4.4 Numerical results at the phase transition

We know that the critical point of the quantum Ising model phase transition, located at

$$C_{Ising} = (t_c, \mu_c) = \left(\frac{1}{2}, 1\right), \tag{4.17}$$

is described by a minimal model with central charge $c = \frac{1}{2}$ following the Table 2.1. Due to this, it is possible to construct the whole Hilbert space by applying operators of the Virasoro subalgebra over descendant states, as well as classify uniquely the theory by the value of c or find the analytical value of its scaling dimensions.

Even though this model is analytically solvable, it is still interesting to approach it numerically in order to demonstrate the methods that we will use in the following chapters. Below we will see how it is possible to compute quantities such as the central charge, the critical exponents or the scaling dimensions of the conformal field theory at the critical point C_{Ising}.

First, we can calculate the central charge from the entanglement entropy using the Calabrese-Cardy formula 3.8. To do so, we calculate the ground states of the Ising model for two different lengths of the chain $L = 50, 100$ using methods available in the TeNPy library. We can see the result in Figure 4.4 (a). We can see how it takes the expected value of $c = \frac{1}{2}$ because the Ising model is described by a free-fermion CFT. Secondly, we can calculate the critical exponent η by fitting the structure factor following the formula 3.12. The result is $2 - \eta = 1.743$ as seen in Figure 4.4 (b). Note how in both cases there is an intersection of the different curves at the point $\mu_c = 2t_c = 1$ given by the scale invariance of the central load $c(L)$ and of the structure factor $S(L)$ at the critical point.

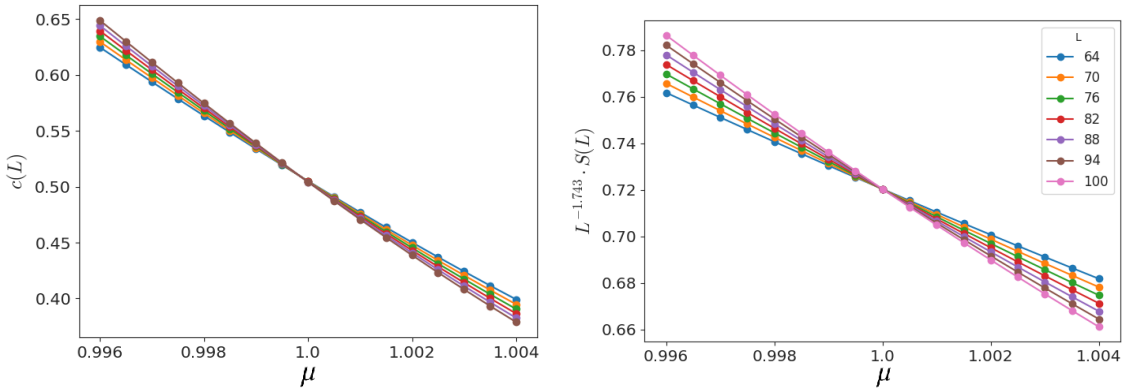

(a) Central charges

(b) Structure factor and critical exponent η

Figure 4.4: Numerical results for the phase transition of the quantum Ising model at C_{Ising} 4.17.

Observable	Numerical value	Ising CFT value	Difference (%)
c	0.5	~0.5	~0.0
$2-\eta$	1.743	1.75	0.05

Table 4.1: Numerical results for the phase transition of the quantum Ising model at C_{Ising} 4.17.

Finally, we can compute the scaling dimensions of the theory by optimizing a MERA and using the conformal information extraction algorithms discussed in the previous chapter. Since it is a minimal model, its analytical values are known in advance so we can try to see if they match. The result is in Figure 4.5, and we see how the values obtained with this algorithm match the exact ones, which gives us confidence regarding the good performance of the MERA for the upcoming models.

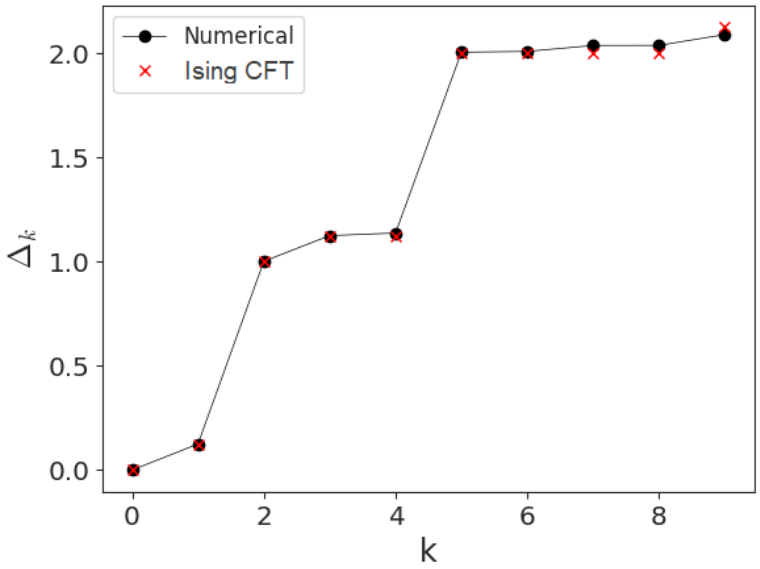

Figure 4.5: Exact and numerical scaling dimensions for the quantum Ising model using MERA.

We see in Table 4.1 as well as on Figure 4.5 how all the numerical values obtained at C_{Ising} are consistent with what is expected: a quantum phase transition characterized by a free-fermion conformal field theory. Therefore, the Kitaev model has served as a good benchmark for testing the numerical methods before applying them to more complicated models.

4.5 Non-Abelian statistics and quantum computation

The Majorana zero modes existing in the topological phase of the Kitaev model present interesting applications in quantum computing due to their properties as non-Abelian anyons. In this section we will explore in more detail these applications as well as the potential experimental implementations of the Kitaev model.

4.5.1 Topological quantum computation with Majorana modes

We will now consider the transformation that the exchange of Majoranas produces on the ground state manifold formed by all the degenerate zero energy states [33, 13]. Suppose we have $2n$ Majoranas forming n pairs. Each Majorana pair gives rise to a fermionic mode, of the form

$$\begin{aligned} c_n^\dagger &= \frac{1}{2}\left(\gamma_{2n-1} + i\gamma_{2n}\right) \\ c_n &= \frac{1}{2}\left(\gamma_{2n-1} - i\gamma_{2n}\right). \end{aligned} \tag{4.18}$$

Each of these modes can be either empty or occupied, giving rise to two possible degenerate states $\{|0\rangle, |1\rangle\}$. In total, we have 2^n quantum states representable by a ket $|s_1, s_2, \ldots, s_n\rangle$ where $s_i = 0, 1$ is the occupation number. This allows us to generate a complete basis of the Hilbert space as

$$|\Psi\rangle = \sum_{s_n=0,1} \alpha_{s_1 s_2 \ldots s_n} |s_1, s_2, \ldots, s_n\rangle \tag{4.19}$$

If we exchange two of the Majoranas γ_n and γ_m, one of the 2^n possible ground states $|\Psi\rangle$ given by 4.19 undergoes a unitary transformation given by $|\Psi\rangle \to U|\Psi\rangle$, where U is now a $2^n \times 2^n$-dimensional matrix. In general, this matrix will take the form

$$U \equiv \exp\left(\beta\gamma_n\gamma_m\right) = \cos(\beta) + \gamma_n\gamma_m \sin(\beta). \tag{4.20}$$

Moreover, going to the Heisenberg picture where we assign the evolution to operators instead of states, it is possible to find out in detail the form of U. In particular, by inserting the operators

$$\begin{aligned} \gamma_n &\to \cos(2\beta)\gamma_n - \sin(2\beta)\gamma_m \\ \gamma_m &\to \cos(2\beta)\gamma_m + \sin(2\beta)\gamma_n \end{aligned} \tag{4.21}$$

it can be shown that the unitary transformations take the form

$$U = \exp\left(\pm\frac{\pi}{4}\gamma_n\gamma_m\right). \tag{4.22}$$

These unitary transformations can in turn represent quantum gates and allow for the development of quantum circuits, as seen in Figure 1.2.

For example, suppose we have a system with four Majoranas $\gamma_1, \gamma_2, \gamma_3, \gamma_4$ and therefore four possible quantum states given by $|00\rangle, |11\rangle, |01\rangle, |10\rangle$. We can induce a unitary transformation on one of these quantum states by interchanging, for example, γ_2 and γ_3 as:

$$U_{23} = \exp\left(\frac{\pi}{4}\gamma_2\gamma_3\right) \equiv \frac{1}{\sqrt{2}}\begin{pmatrix} 1 & -i & 0 & 0 \\ -i & 1 & 0 & 0 \\ 0 & 0 & 1 & -i \\ 0 & 0 & -i & 1 \end{pmatrix}. \tag{4.23}$$

The associated transformation is:

$$|00\rangle \to U_{23}\,|00\rangle = \frac{1}{\sqrt{2}}(|00\rangle - i\,|11\rangle) \tag{4.24}$$

Both the state of the register and the algorithms are topologically protected: the state of the register is encoded in the fermion parity degrees of freedom shared non-locally by the Majoranas, and no local perturbations can cause decoherence. In other words, the environment cannot access the information stored in the Majoranas as long as they are key from each other. On the other hand, the quantum gates represented by the transformations $\exp \frac{\pi}{4}\gamma_n\gamma_m$ are very reliable because they only depend on the relative positions of the Majoranas and not on how this exchange is performed or on their particular trajectory.

Non-universality of Majorana qubits

It is known that it is not possible to implement a universal set of unitary transformations using Majorana / Ising anyons [34]. This means that in order to develop a topological quantum computer that is able to run an arbitrary quantum algorithm, it may be needed to perform non-topological operations, which weakens the main advantage of using anyons namely the topological protection from decoherence. In order to implement arbitrary quantum gates, it is necessary to generalize the Kitaev model so that the associated edge modes exhibit richer non-Abelian statistics, and this is what we will look after in the following sections with parafermion chains.

4.5.2 Experimental realization

It is known that the Kitaev Hamiltonian 4.1 may be potentially realized by means of a wire made of a material with high spin-orbit coupling, placed on top of a superconducting surface and being immersed in a magnetic field, following a disposition such as in Figure 4.6.

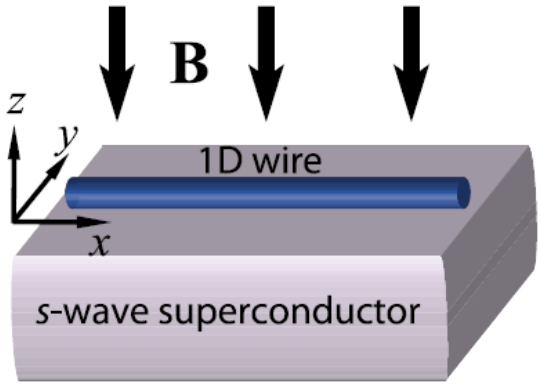

Figure 4.6: Diagram for the experimental realization of the Kitaev model. Retrieved from [33].

This experimental realization requires a highly controllable system so that it can be properly fine-tuned. To this end, a semiconductor material is chosen for the nanowire, which allows to fine-tune the chemical potential μ as the electron density in the semiconductor. Then, the system must be induced with superconductivity in order to introduce the Δ term in the Hamiltonian 4.9. This is done by placing the semiconducting nanowire on top of a superconductor forming a so-called a hybrid structure. Note how this is a daunting challenge from an engineering point of view.

The Kitaev model works with some hypothetical spinless fermions that do not really exist. In order make the model physical, we need to consider that the actual fermions in the chain have spin. Furthermore, the actual Hamiltonian must be expressed by the Pauli matrices σ. In order to add it to the theoretical model, we need to make one of the spin species topologically trivial. This is done by incorporating a Zeeman coupling of the spin to an external magnetic field, and is the reason why a strong spin-orbit coupling is necessary experimentally.

Many efforts have been made to experimentally implement the Kitaev model during the last few years. Most of these experiments have either not found strong enough signatures to prove the existence of Majorana edge modes, or have resulted in false positives that have been later refuted. The main obstacle to realizing these states is believed to be the disorder present in the components used to implement the model, such as nanowire. It is believed that in the foreseeable future, when this disorder can be brought down significantly below current levels, it will be possible to observe signatures of these edge modes [35, 36].

4.6 Interactions: the ANNNI model

A straightforward generalization of the quantum Ising model given by 4.9 is to include an axial interaction compatible with the $\mathbb{Z}_2$ symmetry of the system. This new interaction can consist of a term proportional to $\sigma_i^z \sigma_{i+1}^z$. This results in a Hamiltonian

$$H_{\text{ANNNI}} = -t \sum_{i=1}^{n} \left(\sigma_i^x \sigma_{i+1}^x - \frac{\mu}{2t} \sigma_i^z - \frac{U}{t} \sigma_i^z \sigma_{i+1}^z \right), \tag{4.25}$$

called the Axial Next-Nearest-Neighbours Ising model [37, 38]. It shows a phase diagram as seen in Figure 4.7. The black line for $\frac{U}{t} = 0$ corresponds to the quantum Ising model.

The corresponding Hamiltonian in the fermionic picture is given by:

$$\begin{aligned} H = &\sum_{j=1}^{L-1} \left[-t \left(c_j^\dagger c_{j+1} + c_{j+1}^\dagger c_j \right) + \Delta \left(c_j c_{j+1} + c_{j+1}^\dagger c_j^\dagger \right) \right] \\ &- \frac{1}{2} \sum_{j=1}^{L} \mu_j \left(2n_j - 1 \right) + U \sum_{j=1}^{L-1} \left(2n_j - 1 \right) \left(2n_{j+1} - 1 \right), \end{aligned} \tag{4.26}$$

where we can see that the U term acts as an interaction between the fermion numbers $n_i \equiv c_i^\dagger c_i$.

One of the interesting results of this extension is the appearance of a parametrised line in the phase diagram, along which the system exhibits a very peculiar property. Along this line, called the **Peschel-Emery line**, the Hamiltonian of the system becomes frustration-free, which means that it can be constructed exactly despite the existence of interactions [39]. Phenomenologically, this property can be understood as the disappearance of effects of finite size, such as the energy gap. For this reason, it is expected that by using numerical methods we will obtain exact convergence regardless of the size L of the system.

For this particular model, the Peschel-Emery line is parametrised for the values $\mu = 4\sqrt{U^2 + tU}$ and is represented by the dashed red line.

The Peschel-Emery line is one of the central concepts of this work, since we will see later how it is possible to obtain a similar result for chains of parafermions with two interaction terms in later chapters.

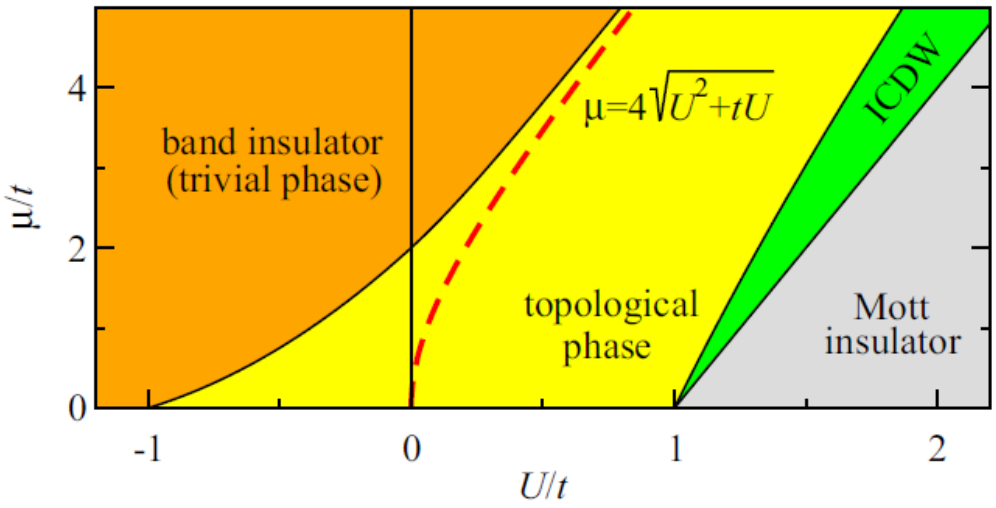

Figure 4.7: Phase diagram for the ANNNI model. Retrieved from [38].

5 | The parafermion chain

As we have seen in the previous chapter, the Kitaev model shows Majorana edge modes in its topological phase. These edge modes are non-Abelian anyons since their spatial exchange produces unitary transformations on the ground state of the system. However, these transformations are limited in the sense that they do not give rise to a universal set of unitary transformations. For this reason, the Kitaev model cannot serve as a basis for the development of topological qubits. However, it is possible to generalise its degrees of freedom, leading to a model whose edge modes give rise to universal quantum gates. The result of this generalisation are entities called parafermions, which will be the focus of this chapter.

For simplicity, we will generalise to the spin picture instead of the fermion picture. Although both ways are equivalent, this makes it easier. In this way, by generalising the spins of the quantum Ising model, we arrive at what is known as the Potts model. Then we can get to the parafermion chain by performing a transformation analogous to the Jordan-Wigner transformation discussed in the previous chapter.

The resulting parafermion model has edge modes in its topological phase, which are also non-Abelian anyons. However, the resulting non-Abelian statistics is more complex and can lead to parafermion structures capable of implementing arbitrary quantum gates with arbitrary precision.

5.1 Introduction

In the previous chapter we saw some features of the Kitaev model, given by the Hamiltonian 4.1. For example, we saw how it is possible to transition to the spin picture by performing a Jordan-Wigner transformation given by 4.8. The result is the quantum Ising model, given by the Hamiltonian 4.9. It has a $\mathbb{Z}_2$ symmetry since it is invariant under the transformation given by

$$\sigma_x \to -\sigma_x, \tag{5.1}$$

which can be seen as invariance under spin sign change.

There are ways to generalise this model. One is to include interactions, as we have seen with the ANNNI model given by the Hamiltonian 4.25. The other, on which we will

focus here, is to change the degrees of freedom of the system itself, for example by modifying the symmetry to which the spins are subjected. This idea was developed by the Australian mathematician Jenfrey Potts in his 1951 thesis [40]. In it, Potts generalises the symmetry present in the quantum Ising model of $\mathbb{Z}_2$ to the general case given by $\mathbb{Z}_q$. Intuitively, the $\mathbb{Z}_q$ symmetry means that the system is invariant under rotations of all spins at a simultaneous angle of $\theta = 2\pi/q$. This is why this type of model is called a clock model.

To perform this generalisation, it is necessary to find a representation of the underlying symmetry group by finding an appropriate representation of the spin matrices of the quantum Ising model. It can be shown how the matrices satisfying this $\mathbb{Z}_q$ symmetry are given by

$$\tau = \begin{pmatrix} 1 & & & \\ & \omega & & \\ & & \ddots & \\ & & & \omega^{q-1} \end{pmatrix}, \qquad \sigma = \begin{pmatrix} & 1 & & \\ & & 1 & \\ & & & \ddots \\ 1 & & & \end{pmatrix}, \tag{5.2}$$

where τ replaces σ^z and σ replaces σ^x in the quantum Ising model. These matrices show an on-site algebra given by

$$\sigma_j^q = \tau_j^q = 1, \quad \sigma_j^\dagger = \sigma_j^{q-1}, \quad \tau_j^\dagger = \tau_j^{q-1}, \quad \sigma_j\tau_j = \omega\tau_j\sigma_j, \quad \omega = e^{2\pi \mathrm{i}/q}, \tag{5.3}$$

while they commute off-site,

$$\left[\tau_i, \tau_j\right] = \left[\sigma_i, \sigma_j\right] = \left[\tau_i, \sigma_j\right] = 0, \quad i \neq j. \tag{5.4}$$

The Hamiltonian resulting from this generalization is given by

$$H = -J \sum_{j=1}^{L-1} \sigma_j \sigma_{j+1}^\dagger - f \sum_{j=1}^{L} \tau_j + \text{H.c.}, \tag{5.5}$$

which is much more complex than the quantum Ising model because it admits chiral terms represented by complex parameters. These terms give rise to time-reversal symmetry and spatial parity breaking. By decomposing the complex parameters into a real part times a phase, this takes the form

$$H = -Je^{-i\theta_J} \sum_{j=1}^{L-1} \sigma_j \sigma_{j+1}^\dagger - fe^{-i\theta_f} \sum_{j=1}^{L} \tau_j + \text{H.c.}, \tag{5.6}$$

where now J and f are real. We see how chirality doubles the number of parameters needed to describe the system.

Many of the most interesting properties of parafermionic systems emerge when considering chiral systems. For example, it is known that chiral parafermion models give rise to strong edge modes [41], which induce degeneracy over the whole spectrum of the system, whereas non-chiral systems give rise to weak edge modes, where the degeneracy only applies to the ground state manifold. For the purpose of this work, however,

we will focus on non-chiral parafermion chains, assuming that the parameters of the Hamiltonian are real. In this case the system 5.5 is called the Potts model.

The simplest non-trivial case is the **three-state Potts model**, where the system has $\mathbb{Z}_3$ symmetry as represented in Figure 5.1 (b). In this case, the above matrices take the form

$$\tau = \begin{pmatrix} 1 & & \\ & \omega & \\ & & \omega^2 \end{pmatrix}, \quad \sigma = \begin{pmatrix} & 1 & \\ & & 1 \\ 1 & & \end{pmatrix}. \tag{5.7}$$

In this case the three-state Potts model has a phase transition at the critical point $f_c = 1$ in a manner analogous to the quantum Ising model. This point is described by a CFT with central charge $\frac{4}{5}$, which is a minimal model.

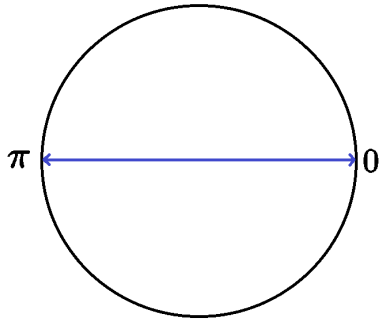

(a) $\mathbb{Z}_2$ symmetry of the Ising model.

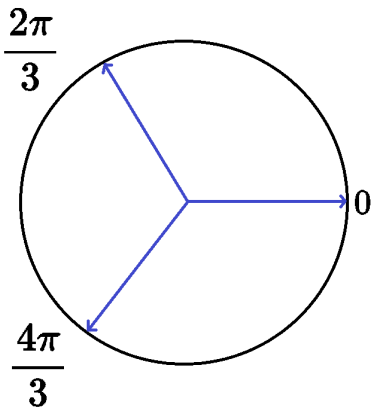

(b) $\mathbb{Z}_3$ symmetry of the Potts model.

Figure 5.1: Representation of local spin symmetries.

5.2 The Fradkin-Kadanoff transformation

We have succeeded in generalising the degrees of freedom of the quantum Ising model to arrive at the three-state Potts model. However, we are interested in studying the effects of this generalisation on the fermion picture. For this purpose we can perform a transformation analogous to the Jordan-Wigner transformation 4.8 to go from the spin picture to the fermion picture. The corresponding expression is called the **Fradkin-Kadanoff transformation**[42] and is given by,

$$\chi_{2j-1} = \left(\prod_{k=1}^{j-1} \tau_k\right) \sigma_j, \quad \chi_{2j} = \left(\prod_{k=1}^{j-1} \tau_k\right) \sigma_j \tau_j = \chi_{2j-1} \tau_j \tag{5.8}$$

If we apply this transformation to the Potts model 5.5, we obtain a system composed of

new degrees of freedom,

$$H = -J \sum_{j=1}^{L-1} \chi_{2j} \chi_{2j+1}^{\dagger} - f \sum_{j=1}^{L} \chi_{2j-1}^{\dagger} \chi_{2j}, \tag{5.9}$$

called the **parafermion chain** [41]. The exchange statistics of parafermions differ from those of fermions and are given by

$$\begin{aligned} &\chi_l^3 = 1, \quad \chi_l^{\dagger} = \chi_l^2 \\ &\chi_l \chi_m = \omega^{\mathrm{sgn}(m-l)} \chi_m \chi_l \quad \text{for } m \neq l, \quad \omega = e^{2\pi i/3}. \end{aligned} \tag{5.10}$$

This new algebra prevents the analytical treatment of parafermion chains, since they are no longer quadratically solvable. For this reason, there are actually no *free* parafermion chains, and it is not accurate to speak of interacting parafermion chains. Furthermore, as we will see below, these models are compelling because, like in the Kitaev model, they exhibit a topological phase which yields parafermionic edge modes with a complex non-Abelian statistics.

5.3 Numerical results at the phase transition

As we saw in the second chapter when discussing conformal field theories, the critical point of the Potts model is a minimal model that can be described by a CFT with central charge $c = \frac{4}{5}$ according to the Table 2.1.

This model forms the basis for the next two models discussed in the following chapters. Therefore, it is of interest to analyse numerically its phase transition at the critical point, located at

$$C_{Potts} = (J_c, f_c) = (1, 1). \tag{5.11}$$

Unlike the Kitaev model, we have seen how the parafermion model 5.9 is **no longer analytically tractable**, since there are no analytical techniques such as the Bogoliubov transformation to express it in terms of non-interacting systems. This forces us to use numerical methods.

Following the same procedures as in the case of the Kitaev model, we proceed to calculate the phase transition numerically using DMRG at the point C_{Potts} 5.11. In Figure 5.2 (a) we can see the values of the central charge obtained by the entanglement entropy; in Figure 5.2 (b) we see the values of the energy gaps and the critical exponent $z = 1$; and in Figure 5.2 (c) we see the values of the structure factor as well as the critical exponent η.

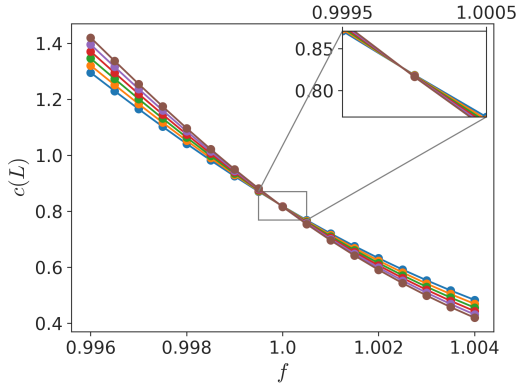

(a) Central charges

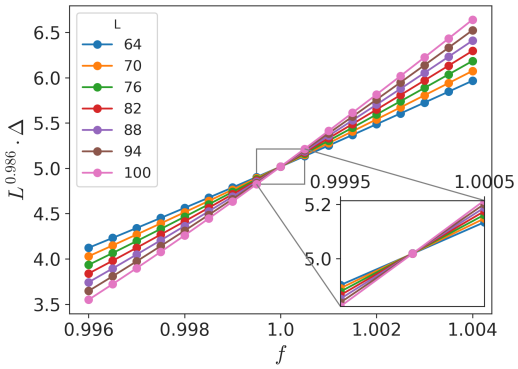

(b) Energy gaps and critical exponent z

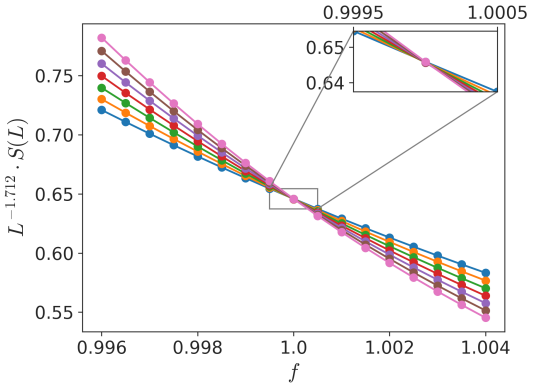

(c) Structure factor and critical exponent η

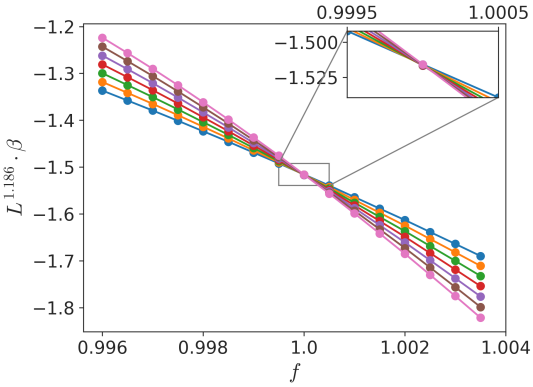

(d) Callan-Symanzik β and critical exponent ν

Figure 5.2: Results for the 3-state Potts model at the critical point C_{Potts} 5.11.

Observable	Numerical value	Potts CFT value	Difference (%)
c	0.82	0.8	2.5
z	0.986	1	1.4
$2-\eta$	1.712	1.733	1.2
$1/\nu$	1.186	1.2	1.2

Table 5.1: Results for the 3-state Potts model at the critical point C_{Potts} 5.11.

Finally, we can calculate the scaling dimensions using the MERA. As this is a minimal model, the theoretical values are known, which allows us to add an additional check to the model. As we can see in Figure 5.3, these values are very close to what is expected.

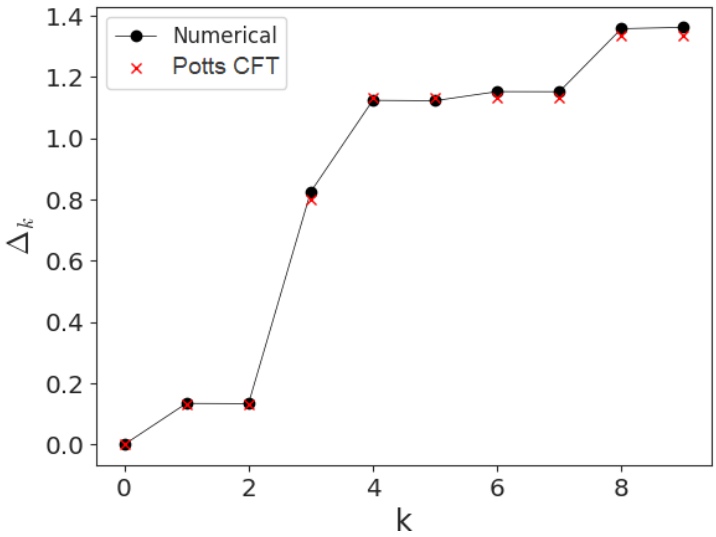

Figure 5.3: Potts-CFT and numerical scaling dimensions at the point C_{Potts}.

As we can see both in Table 5.1 and in 5.3, all the results obtained are consistent with a quantum phase transition characterized by a Potts minimal model: the central charge takes the value $c = \frac{4}{5}$, and the critical exponents as well as scaling dimensions are close to those of the Potts conformal field theory.

5.4 Non-Abelian statistics and quantum computation

As we saw in the previous chapter with the Kitaev model, the anyonic properties associated with edge modes in the topological phase show applications in quantum computing. However, Majorana zero modes can only give place to a limited set of unitary transformations in the system, meaning that the possible quantum computation is not universal.

For the edge modes associated with parafermion chains, it can be shown how this is no longer the case. In particular, it is possible to construct anyon models that lead to universality from the non-Abelian anyons of parafermion chains, among the simplest of which is the **Fibonacci anyon model** [8, 43]. This implies that these anyon models can be used to approximate any unitary transformation with arbitrary precision, which could lead to the realisation of quantum circuits such as the one shown in Figure 1.2.

6 | The parafermion chain with one extension

In this chapter we will discuss an extension of the parafermion chain seen in the previous chapter. This generalisation is given by the extension of the Hamiltonian with term depending on a new parameter, and is motivated by a possible experimental realisation of the resulting model. The resulting phase diagram is extended to two dimensions and exhibits a wide variety of topological and exotic phases.

We will see how the resulting model is analogous to the ANNNI model discussed as a generalization the Kitaev model, and indeed shares some of its properties.
Due to the difficulty of analysing this system analytically, the exploration of the phase diagram must be carried out mainly by means of the numerical methods discussed in the previous chapters. This exploration, consisting in the use of DMRG and MERA, allows for the characterisation of its different phases and the representation of its phase diagram.

6.1 Introduction

In the previous chapter we saw how the Potts model arises after generalising the underlying symmetry of the quantum Ising model from $\mathbb{Z}_2$ to $\mathbb{Z}_q$. We saw how the resulting model admits chiral terms that can be expressed by complex parameters, leading to the model 5.6. However, we restricted it to the three-state Potts model with real parameters given by 5.5. Finally, we saw how this model can be expressed as a parafermion chain after performing a Fradkin-Kadanoff transformation given by 5.9.
In this chapter we generalise this parafermion chain by extending the three-state Potts model Hamiltonian with a term proportional to a new parameter U. This model allows this extension because the Z_3 symmetry is preserved. The resulting Hamiltonian is given by

$$H = -J \sum_{j=1}^{L-1} \sigma_j \sigma_{j+1}^{\dagger} - f \sum_{j=1}^{L} \tau_j + U \sum_{j=1}^{L-1} \tau_j \tau_{j+1} + \text{ H.c. }, \tag{6.1}$$

where in the following unless stated otherwise we set $J = 1$. This model has been studied in detail by J. Wouters et al. in the paper *Phase diagram of an extended parafermion chain* [1]. In the following we will summarise some of the results obtained in this work, focusing in particular on the upper part of the phase diagram for $f \geq 1$, where the system shows a topological and trivial phase extension of the parafermion chain described

in the previous chapter.

We can see how the Hamiltonian 6.1 is analogous to the ANNNI model seen in Chapter 4 and given by the Hamiltonian 4.25, but with $\mathbb{Z}_3$ symmetry instead of $\mathbb{Z}_2$. For this reason, this model is called the **Axial Next-Nearest-Neighbours Potts model** (ANNNP). In this chapter we will see how this model possesses some of the qualities of the ANNNI model, such as the possession of two points corresponding to the intersection with a Peschel-Emery line along which the system is frustration-free. However, we will see that there are also some differences, namely that the full parametrised line is not fully contained by this model, and that it is necessary to introduce a second extension into it in order to do it. This will be the subject of the next chapter.

6.2 The Fradkin-Kadanoff transformation

We can transform the ANNNP model given by 6.1 by transforming it into its fermion image by the Fradkin-Kadanoff transformation 5.8. The resulting parafermion model is

$$H = -J\sum_{j=1}^{L-1}\chi_{2j}\chi_{2j+1}^{\dagger} - f\sum_{j=1}^{L}\chi_{2j-1}^{\dagger}\chi_{2j} + U\sum_{j=1}^{L-1}\chi_{2j-1}^{\dagger}\chi_{2j}\chi_{2j+1}^{\dagger}\chi_{2j+2} + \text{ H.c. }. \tag{6.2}$$

We see how the term proportional to the parameter U incorporates interactions beyond the first neighbours in a reminiscent way as to how the ANNNI model did in 4.26. The parameters J, f and U are assumed to be real, making the model non-chiral.

Again, although it is tempting to call this model an interacting parafermion chain, it is not entirely accurate since the model with $U = 0$ is not a free model and also has interactions.

6.3 Phase diagram

The phase diagram corresponding to the ANNNP model 6.1 significantly extends that of the Potts model 5.5, leading to an extension of the topological and trivial phases at the top of the phase diagram for $f \geq 1$, and to a set of "exotic" phases for $f < 1$. We can see this in Figure 6.1.

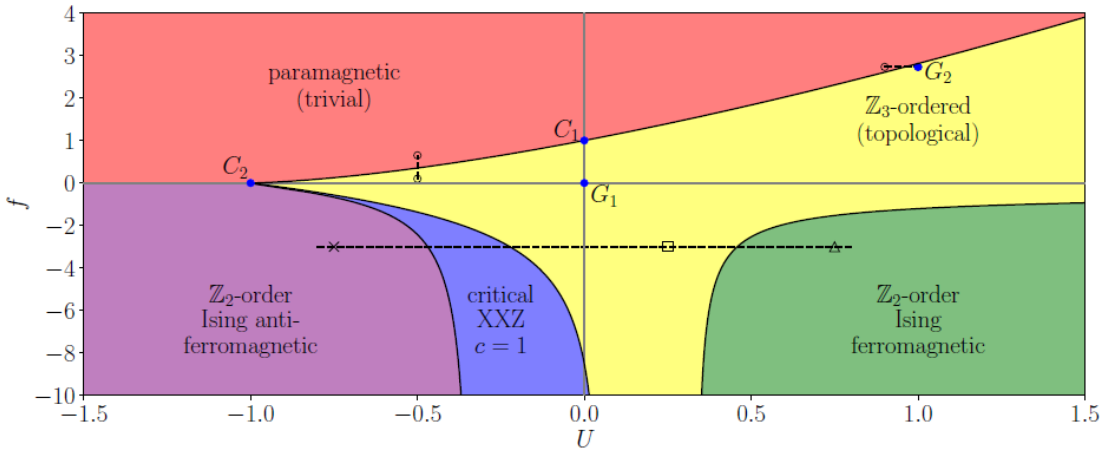

Figure 6.1: Phase diagram of 6.1. Extracted from [1]

This phase diagram is characterised by the appearance of two fixed points, C_1, corresponding to a Potts-type phase transition characterised by a CFT with central charge $\frac{4}{5}$, and C_2, corresponding to a more complex phase transition characterised by a CFT with central charge $\frac{8}{5}$, which can be understood as two copies of the Potts model [1].

At the same time we can see how two other points G_1 and G_2 appear in the phase diagram, corresponding to the intersections with a Peschel-Emery line that lies in an extended model. All of these points are summarised in Formula 6.3 (notice how J is set to 1).

$$\begin{aligned} C_1 &= (f, U) = (1, 0) \\ C_2 &= (0, -1) \\ G_1 &= (0, 0) \\ G_2 &= (1 + \sqrt{3}, 1) \\ \tilde{C}_3 &= G_2 - (0, 0.32) = (1 + \sqrt{3}, 0.968) \end{aligned} \tag{6.3}$$

6.4 Numerical results at the phase transition

In this section we analyse the phase transition of the ANNNP model at a point far away from the critical point C_1, in order to better appreciate the effects of the U term. In particular, we will analyse the phase transition located right next to the intersection of the Peschel-Emery line at G_2, at a point labelled as $\tilde{C}_3$ in 6.3. Furthermore, we will perform the computations through a horizontal slice around the point $\tilde{C}_3$ by ranging the U parameter instead of the f parameter as done in the last chapter. This emphasizes the influence of the U term but prevents us from calculating the Callan-Symanzik function 3.13 since we do not have the value of $\frac{\partial \Delta}{\partial \ln f}$.

If the transition at this point is also of Potts type, then using renormalisation group arguments we can expect the entire intermediate critical line to be of Potts type as well.

In particular, the c-theorem states that if the central charge takes two different values at both critical points, then it will undergo a monotonic transition along all intermediate values.

To this end, we calculate some observables for the phase transition at a point on the critical line at $\tilde{C}_3$. In Figure 6.2 (a) we can see the values of the central charge. We see that it takes a value close to $c = 0.9$, which deviates considerably from the exact value of $c = 0.8$. On the other hand, Figure 6.2 (b) corresponds to the critical exponent associated with the energy gap. We see how we obtain a value $z = 0.873$, which also deviates noticeably from $z = 1$. In Figure 6.2 (c) we see the critical exponent $2-\eta$ associated with the structure factor S. Notice how in this case we do not have a Figure for the Callan-Symanzik β function since we are performing an horizontal cut with respect to the U parameter, and it is not possible to compute it following expression 3.13. All this data is presented in Table 6.1.

The results obtained are not as close as those of the previous chapters for the phase transition of the parafermion chain at point C_{Potts}. This may be due to several reasons. One of them is the fact that, being further away from the critical point, there are perturbations corresponding to the different interactions which affect the numerical values. The other may have something to do with the fact that an analysis is carried out with respect to the parameter U.

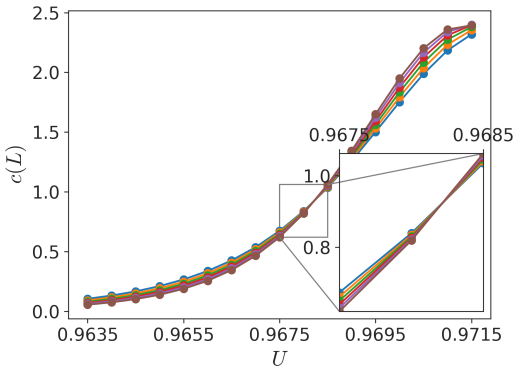

(a) Central charges

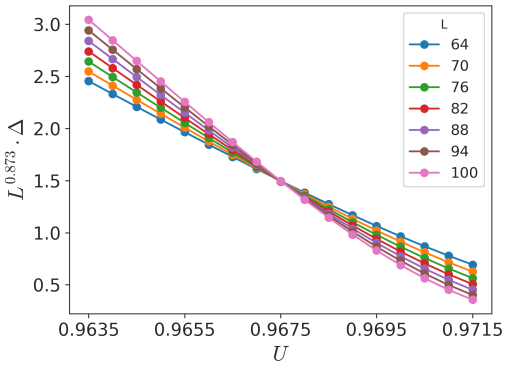

(b) Energy gaps and critical exponent z

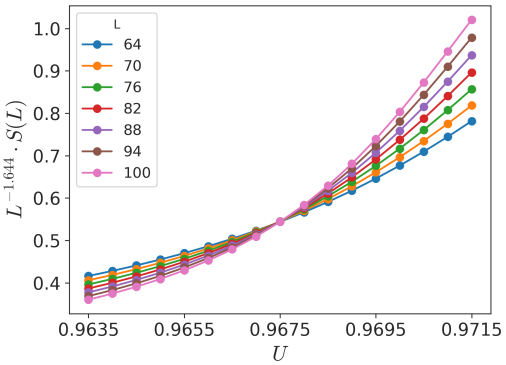

(c) Structure factor and critical exponent η

Figure 6.2: Results for the ANNNP model at $\tilde{C}_3$ 6.3.

Observable	Numerical value	Potts CFT value	Difference (%)
c	0.9	0.8	12.5
z	0.873	1	13.7
$2-\eta$	1.644	1.733	8.9

Table 6.1: Results for the ANNNP model at $\tilde{C}_3$ 6.3.

Finally, in figure 6.3 we see the values for the scaling dimensions of the transition at this point using MERA. We see how these are reasonably close to the exact values, but are somewhat farther away from those obtained for the case of the previous parafermion model.

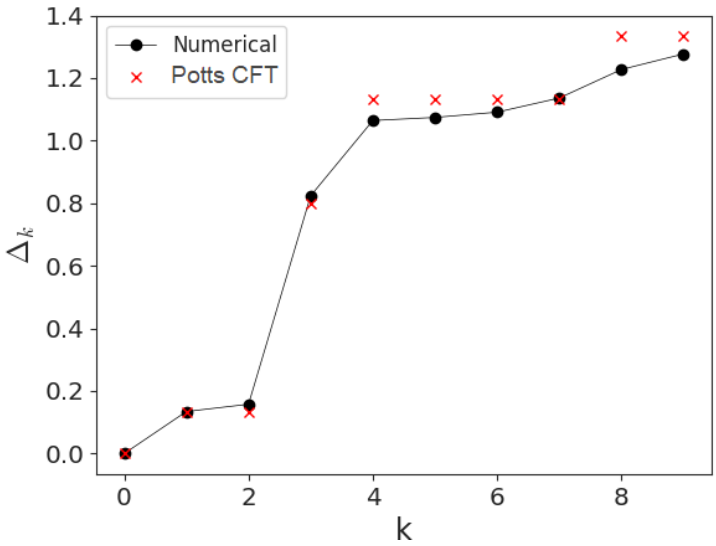

Figure 6.3: Exact and numerical scaling dimensions using MERA at $\tilde{C}_3$ 6.3.

These results still seem to indicate that the phase transition around $\tilde{C}_3$ is still characterized by a Potts CFT, but they are not as robust as those obtained in the previous chapter. This may be due to several reasons. The first of these may simply be a poor convergence of the methods employed. It is possible that the bond dimension χ of both the Matrix Product States for the DMRG and MERA cases is not high enough to fully capture the quantum correlations in $\tilde{C}_3$, which may be enhanced by the influence of the U term. The second of these reasons may be given by the use of the U parameter instead of f when performing the slices for finite-size scaling. Finally, it may be that the data is influenced by the existence of a phase transition of a different type than the Potts CFT, although we find this unlikely since a priori we do not expect a critical point in the vicinity of $\tilde{C}_3$.

6.5 Non-Abelian statistics and quantum computation

One of the main motivations for introducing an extension term in the parafermion model is a possible experimental realisation of the model, since it may be possible to implement 6.2 experimentally by restricting the boundary quantum states of interacting systems in two dimensions [1, 44]. In particular, a heterostructure composed of superconductors combined with ferromagnets would allow the generation of fractional quantum Hall states with filling factors ν and could implement the model as we can see in Figure 6.4.

To carry out this realisation, it is necessary to include an extension term associated with the parameter U, so that the effective Hamiltonian $H_J + H_f + H_U$ corresponds to the one presented in 6.1.

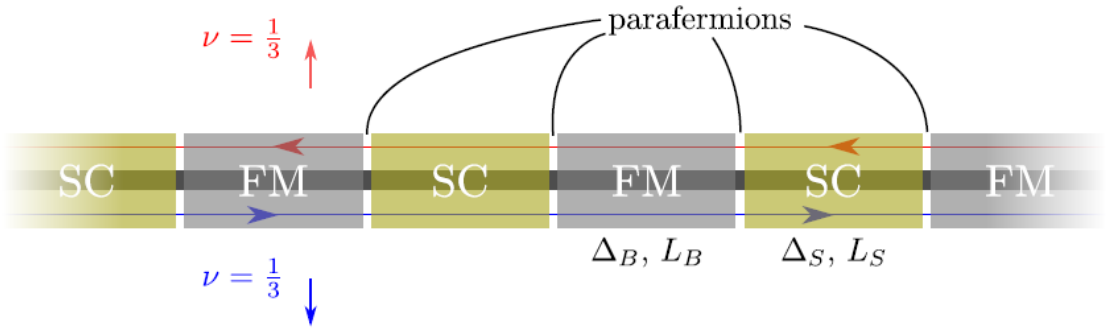

Figure 6.4: Diagram of the potential experimental realization with gaps given by Δ and lengths L. Extracted from [1]

7 | The parafermion chain with two extensions

In this chapter we will study a generalization of the parafermion chain shown in the previous chapter by incorporating an additional extension term in its Hamiltonian. Such a term can be incorporated as long as it preserves the $\mathbb{Z}_3$ symmetry of the ANNNP model.

The motivation for this extension is that the resulting model contains a parametrised line, called the Peschel-Emery line, along which the Hamiltonian of the system becomes frustration-free and thus shows an exact degeneracy of the fundamental state for any chain length. Phenomenologically, this means that along this parametrised line the energy gap closes for any chain length. We will see how the expression for this Peschel-Emery line can be derived from an argument originally proposed by E. Witten to analyse supersymmetric quantum field theories.

Finally, we will conclude this work by summarizing all the results found for the model into a three-dimensional phase diagram.

7.1 Introduction

The parafermion chain with two extensions arises from a generalization of the ANNNP 6.1 model seen in the previous section. In particular, it is possible to incorporate a term in the form $\tau_j \tau_{j+1}^\dagger$ dependent on a parameter V that preserves the $\mathbb{Z}_3$ local symmetry to achieve a Hamiltonian in the form

$$H = -J \sum_{j=1}^{L-1} \sigma_j \sigma_{j+1}^\dagger - f \sum_{j=1}^{L} \tau_j + U \sum_{j=1}^{L-1} \tau_j \tau_{j+1} + V \sum_{j=1}^{L-1} \tau_j \tau_{j+1}^\dagger + \text{ H.c.} \tag{7.1}$$

The motivation behind this extension is that it accommodates a line in parameter space, called the **Peschel Emery line**, along which the Hamiltonian is frustration-free [45]. This means that, along this line, it is possible to construct the ground state exactly, even analytically. Practically, the frustration-free effects are manifested as an exact closing of the energy gap.

7.2 Numerical results at the phase transition

The result of this generalisation is an extension of the phase diagram seen in Figure 6.1 in the form of a new dimension with respect to the parameter V. Thus, the phase diagram 6.1 becomes a two-dimensional slice of the generalized, three-dimensional parameter space.

Our aim for this chapter is to analyse the properties of the phase transitions for a finite value of V. First, we can compute the location of the two-dimensional surface separating the trivial and topological phases accounting for the extra dimension. A way to do so is by computing the entanglement entropy and/or the central charges in an approximate way along the plane described by the f and U parameters for different values of V. This allows us to find the changes of the critical line as a function of V and to fit the critical plane.

The approximated values for the central charge and the entanglement entropy can be seen in the Figures 7.1 and 7.2. We see how the critical line rises in the diagrams as a function of V.

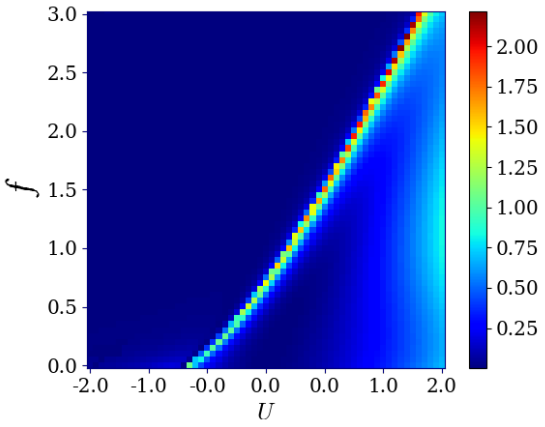

(a) $V = -0.2$

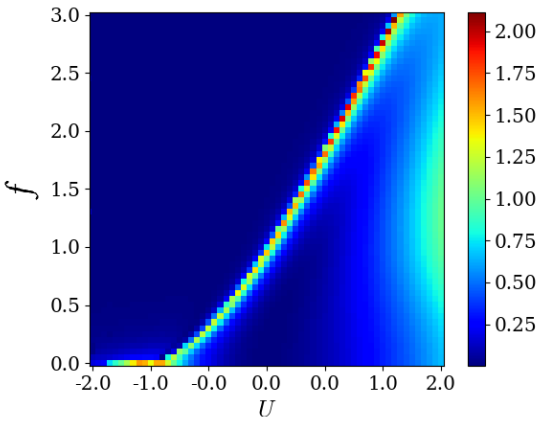

(b) $V = 0$

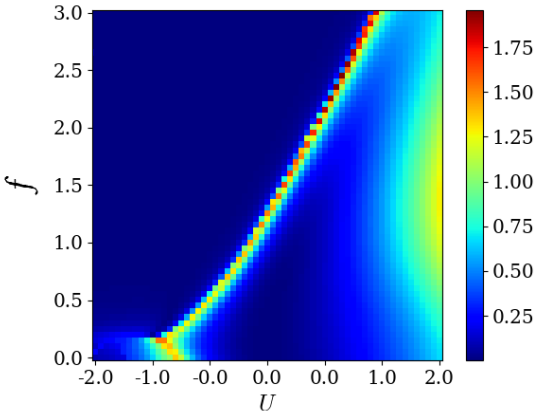

(c) $V = 0.2$

Figure 7.1: Entanglement entropy along the fU plane.

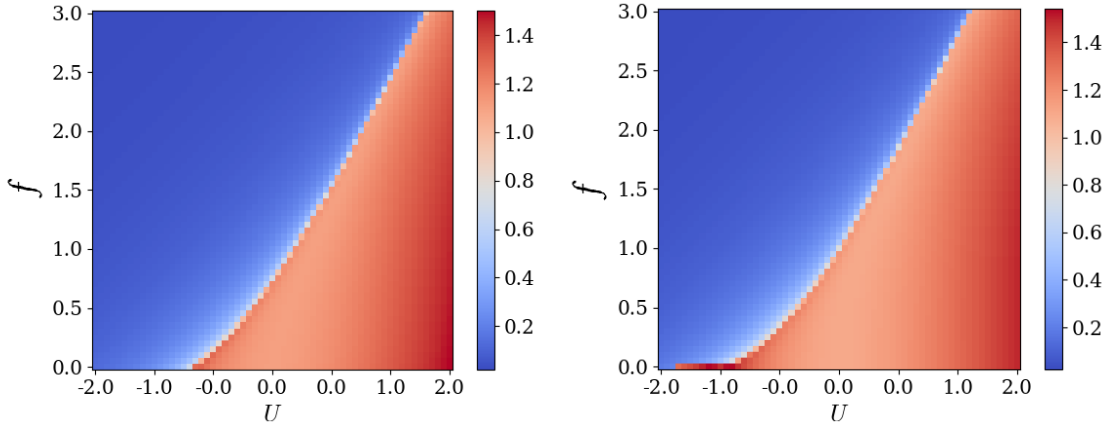

(a) $V = -0.2$

(b) $V = 0$

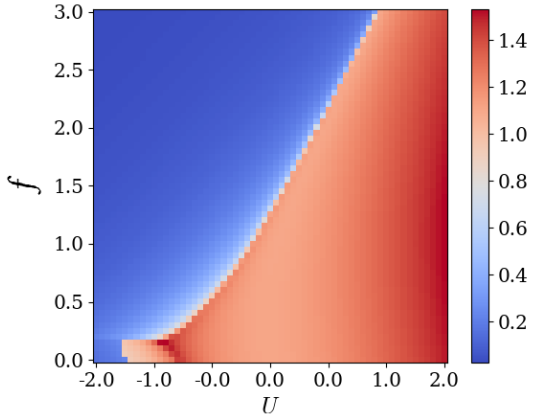

(c) $V = 0.2$

Figure 7.2: Central charges along the fU plane.

From these points, we can fit a critical plane that separates the topological phase from the trivial one, as seen in Figure 7.3. First of all, if we simply fit a plane to the points provided by the rough topographies, we obtain the equation

$$f_c(U, V) = 0.913 + 1.829U + 1.649V. \tag{7.2}$$

This is not a perfect fit since it does not contain the point $f_c(0, 0) = 1$. However, if we instead consider a quadratic surface and we force this condition then we obtain the equation:

$$f_c(U, V) = 1 + 1.591U + 1.653V + 0.155U^2 - 0.323V^2 \tag{7.3}$$

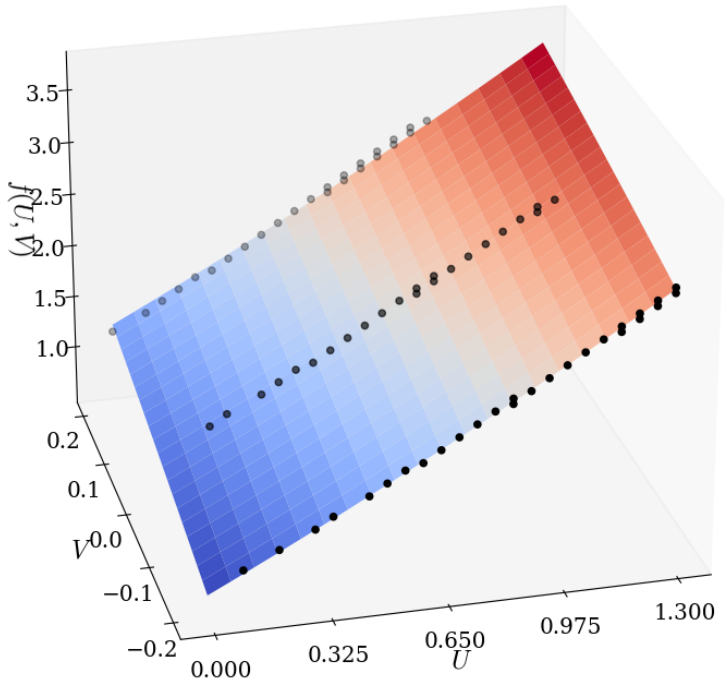

Figure 7.3: Quadratic critical surface fitted from 7.3

The next thing we can do is to compute the finite size-scaling of several observables given a finite value of V, and check if the results are consisten with a Potts quantum phase transition.

To this end, we apply the numerical methods at a point close to the intersection of the Peschel-Emery line at G_2 but with a finite value of V, which we label as $\tilde{C}_4$.

$$\tilde{C}_4 = (f, U, V) = G_2 + (0.791, 0, 0.4) = (3.522, 1, 0.4). \tag{7.4}$$

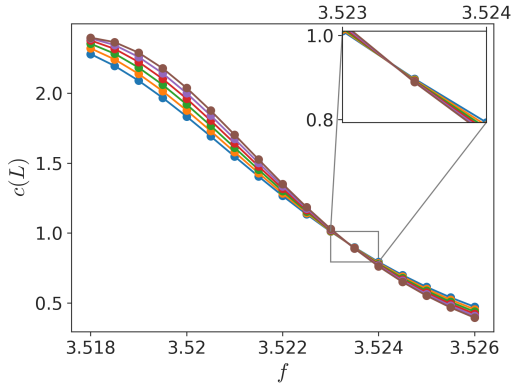

(a) Central charges

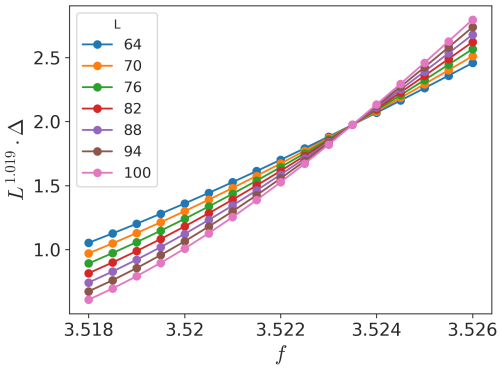

(b) Energy gaps and critical exponent z

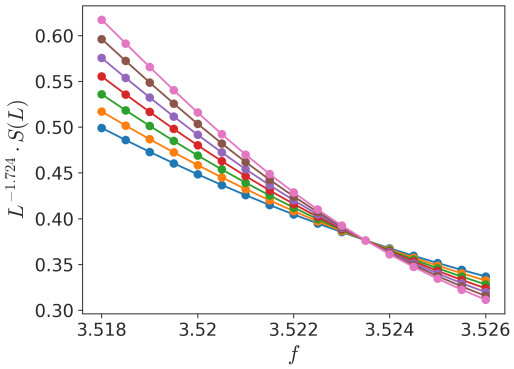

(c) Structure factor and critical exponent η

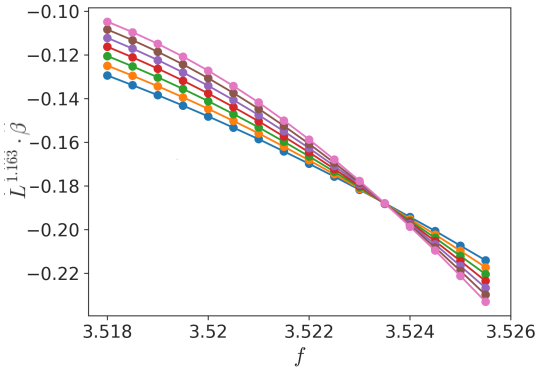

(d) Callan-Symanzik β and critical exponent ν

Figure 7.4: Results for the extended ANNNP model at $\tilde{C}_4$ 7.4.

Observable	Numerical value	Potts CFT value	Difference (%)
c	0.86	0.8	7.5
z	1.019	1	1.9
$2-\eta$	1.724	1.733	0.5
$1/\nu$	1.163	1.2	3

Table 7.1: Results for the extended ANNNP model at $\tilde{C}_4$ 7.4.

The values obtained are shown in Figure 7.4 and Table 7.1. There, we can see how the critical exponents resemble what is expected for a Potts CFT. Actually, these results for a finite value of V resemble it closer than those shown in the previous chapter for $V = 0$. However, the central charge still deviates a bit from the expected value. This gives us confidence when it comes to evaluate the phase transition along the entire critical surface as of Potts type.

As can be seen in Figure 7.5, although these dimensions are within approximately the appropriate ranges, they are clearly off from their exact values given by the Potts CFT. As

the DMRG results in 7.1 suggest that the transition is still described by a Potts theory, it is likely that this is due to a convergence problem, for example due to a bond dimension value that is too small to properly capture the correlations of the model at this point.

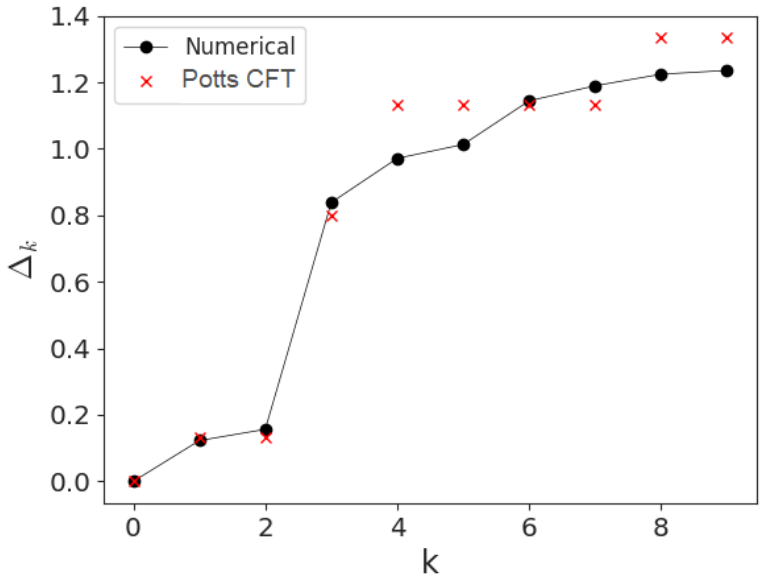

Figure 7.5: Exact and numerical scaling dimensions using MERA at $\tilde{C}_4$ 7.4.

Given all these results, one can reasonably suspect that the phase transition along the entire critical surface given by (f_c, U_c, V_c) is characterized by a Potts CFT.

7.3 The Witten conjugation argument

It is possible to construct frustration-free lines using the Witten conjugation argument [46]. This argument, originally introduced in the context of supersymmetric quantum mechanics models, makes possible to construct a Hamiltonian $\tilde{H}$ with the same number of zero-energy states as a deformation of another Hamiltonian H whose properties are known. In our particular case, we can apply it to the extended ANNNP model 7.1 to write it as a deformation of a simpler Hamiltonian and, in this way, find its relevant frustration-free line.

In essence, this argument states that given a Hamiltonian in the form

$$H = \sum_{j=1}^{N-1} H_{j,j+1} = \sum_{j=1}^{N-1} L_{j,j+1}^{\dagger} L_{j,j+1}, \tag{7.5}$$

where each term acts non-trivially on neighbouring terms and is positive semi-definite, we can act with an invertible operator M_j on the local Hilbert spaces at the site j, such that we act on the whole chain with an operator $M = \prod_j M_j$. Thus, we can write the conjugate operators as

$$\tilde{L}_{j,j+1} = M_j M_{j+1} L_{j,j+1} M_{j+1}^{-1} M_j^{-1}, \tag{7.6}$$

and the conjugate Hamiltonian as

$$\tilde{H} = \sum_{j=1}^{N-1} \tilde{H}_{j,j+1} = \sum_{j=1}^{N-1} \tilde{L}_{j,j+1}^{\dagger} C_{j,j+1} \tilde{L}_{j,j+1}, \tag{7.7}$$

where we have introduced the positive-definite operator $C_{j,j+1} = K_{j,j+1}^{\dagger} K_{j,j+1}$ as an additional degree of freedom in the construction.

Then, we can state the following theorem.

Theorem: *The ground-state manifold $\tilde{G}$ of the conjugated Hamiltonian $\tilde{H}$ is given by $\tilde{G} = \mathrm{span}\{M|\Psi_1\rangle, \ldots, M|\Psi_n\rangle\}$, thus the ground-state degeneracies of H and $\tilde{H}$ are identical.*

The proof can be found at [46]. This gives us a straightforward way to calculate the degeneracy of the ground state of the deformed Hamiltonian, without making any statements about the energy gap above the ground state.

There exist some degrees of freedom when choosing $L_{j,j+1}$, $C_{j,j+1}$ and M_j, given by possibility of performing a local basis transformation by means of an operator $V_j = 1 \otimes \ldots \otimes 1 \otimes v_j \otimes 1 \otimes \ldots \otimes 1$ as:

$$\begin{aligned} M_j &\to V_j M_j V_j^{\dagger}, \\ L_{j,j+1} &\to V_j V_{j+1} L_{j,j+1} V_j^{\dagger} V_{j+1}^{\dagger}, \\ C_{j,j+1} &\to V_j V_{j+1} C_{j,j+1} V_j^{\dagger} V_{j+1}^{\dagger}. \end{aligned} \tag{7.8}$$

Using this freedom, we can choose a suitable basis in the local Hilbert spaces to simplify the different operators. For example, we can apply this argument to the extended ANNNP model with real coefficients by taking the operators

$$m_j = \begin{pmatrix} 1 & & \\ & r & \\ & & r \end{pmatrix}, \quad L_{j,j+1} = \sigma_j - \sigma_{j+1}, \quad C_{j,j+1} = K_j K_{j+1}, \quad k_j = \begin{pmatrix} r & & \\ & 1 & \\ & & r^{-1} \end{pmatrix}, \tag{7.9}$$

where $M_j = 1 \otimes \ldots \otimes 1 \otimes m_j \otimes 1 \otimes \ldots \otimes 1$ and $K_j = 1 \otimes \ldots \otimes 1 \otimes k_j \otimes 1 \otimes \ldots \otimes 1$ are diagonal in the τ-basis.
Then, it can be shown how the deformed Hamiltonian takes the simple form

$$\tilde{H} = -\sum_j \left[\sigma_j \sigma_{j+1}^{\dagger} + \frac{f}{2}\left(\tau_j + \tau_{j+1}\right) - U\tau_j\tau_{j+1} - V\tau_j\tau_{j+1}^{\dagger} + \text{ H.c.} \right], \tag{7.10}$$

and the frustration-free line gets specified by the coefficients given by

$$\begin{aligned} f &= \frac{2(1+2r)\left(1-r^3\right)}{9r^2} \\ U &= \frac{2(1-r)^2\left(1+r+r^2\right)}{9r^2} \\ V &= -\frac{(1-r)^2\left(1-2r-2r^2\right)}{9r^2}. \end{aligned} \tag{7.11}$$

This is known as the **Peschel-Emery line**, and is of the same nature as the one shown by the ANNNI model.

7.4 Frustration-free effects

We can calculate the implications of frustration-free effects along the Peschel-Emery line 7.11 numerically. Indeed, using DMRG we see how the gap closes exactly along these points. To do so, we check the effects at three different points in the phase diagram: G_1, G_2 and a third point which we will call $\tilde{G}_3$ which will be in between, belonging to the space with a finite value of V as seen in 7.12.

$$\begin{aligned} G_1 &= (f,U,V)(r=1) = (0,0,0) \\ G_2 &= (f,U,V)(r=0.37) = (1+\sqrt{3},1,0) \\ \tilde{G}_3 &= (f,U,V)(r=0.5) = (1.556, 0.389, 0.056) \end{aligned} \tag{7.12}$$

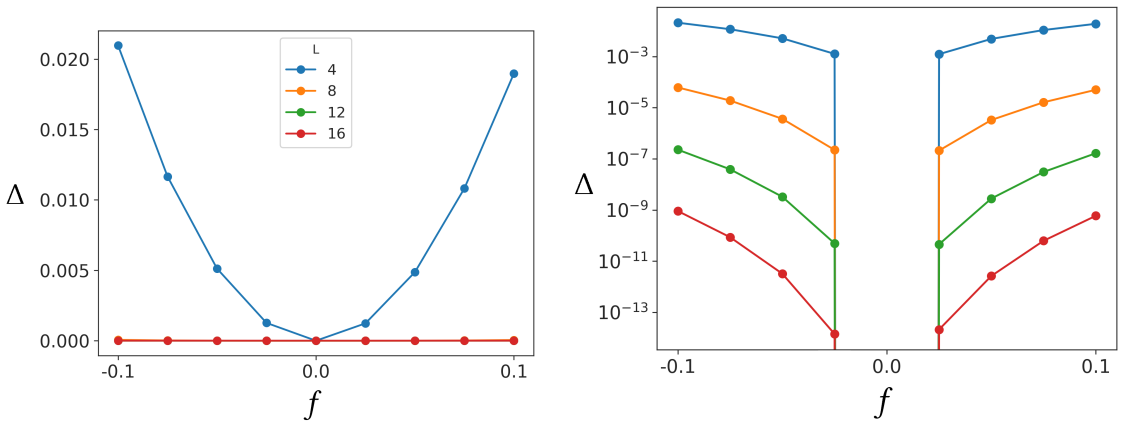

(a) Cut along the f parameter

(b) Cut along the f parameter in log scale

Figure 7.6: Frustration-free effects at G_1 7.12.

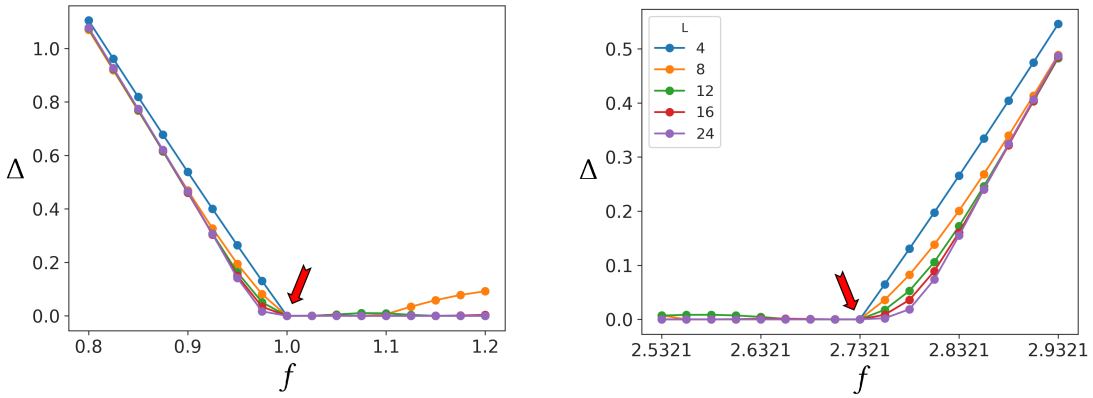

(a) Cut along the f parameter

(b) Cut along the U parameter

Figure 7.7: Frustration-free effects at G_2 7.12, with the Peschel-Emery line intersection highlighted.

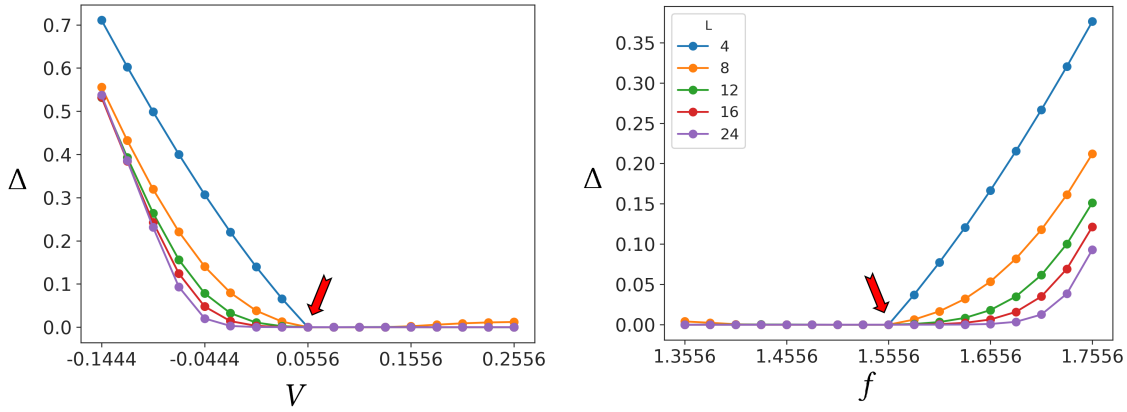

(a) Cut along the f parameter

(b) Cut along the U parameter

Figure 7.8: Frustration-free effects at $\tilde{G}_3$ 7.12, with the Peschel-Emery line intersection highlighted.

7.5 Phase diagram

Finally, by putting everything together, we can unify the phase diagram into a single figure and draw the different phases we have identified.

In the Figures 7.9, 7.10 and 7.11 we can appreciate the front, back and top views of the extended phase diagram respectively. We can appreciate how the Peschel-Emery line remains at all times inside the topological phase and how the critical plane separates the trivial and topological phases.

Given the data obtained in the table 7.1, we can expect the phase transition along the critical surface fitted by the formula 7.3 to be of the Potts type at all its points, at least for moderate values of the parameters (f, U, V).

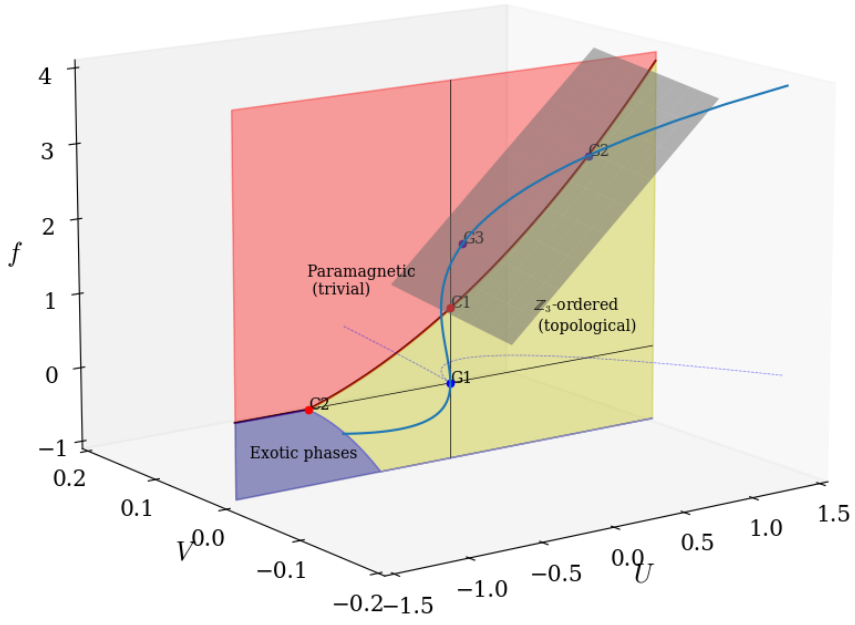

Figure 7.9: Front view of the phase diagram

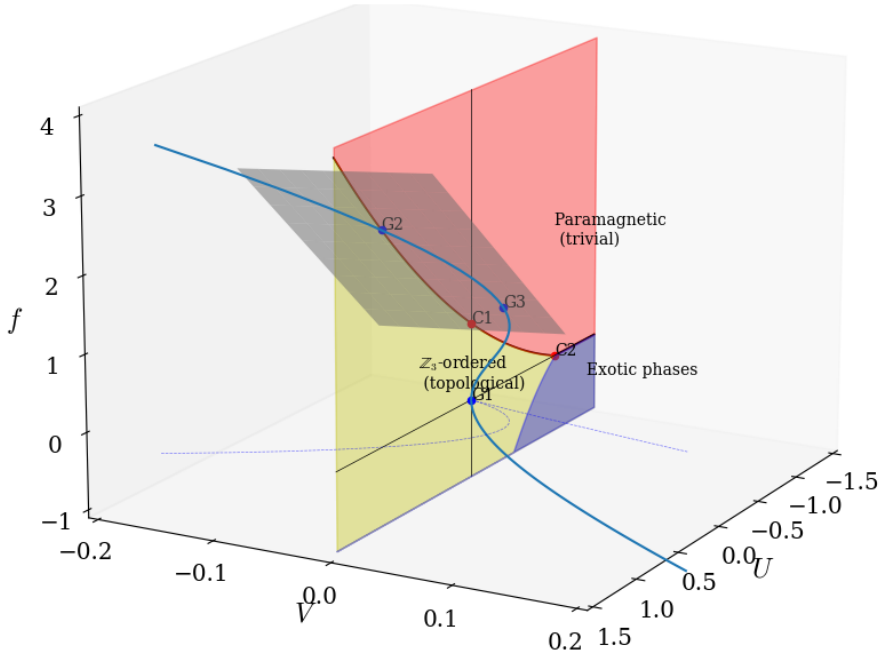

Figure 7.10: Back view of the phase diagram

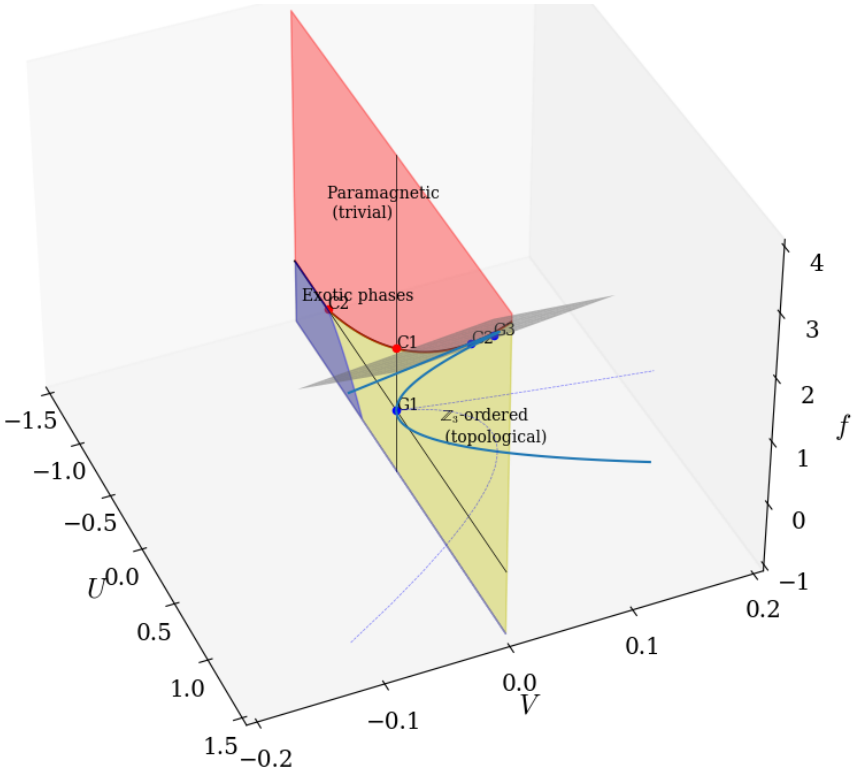

Figure 7.11: View from above of the phase diagram

8 | Discussion

In this work we have studied the phase diagram corresponding to different one-dimensional quantum systems. First of all, we introduced and explained the approach followed for the rest of the work, which consists of several techniques, both analytical and numerical. Then, as a starting point, we introduced the Kitaev model and its spin dual, the quantum Ising model. We then generalised the local $\mathbb{Z}_2$ symmetry of the quantum Ising model to arrive at the 3-state Potts model and its corresponding parafermion chain. Finally, we introduced extension terms in the Hamiltonian of the parafermion chain to arrive at more general models with a richer phase diagram.

In essence, we have been able to characterise a collection of one-dimensional quantum models that exhibit topological properties. At the same time, we have been able to look more closely at the implications of these properties, ranging from their possible applications in quantum computing to possible experimental realisations. We have seen how they can be used to protect, store and process quantum information, the limitations of this paradigm for topological quantum computation when using Ising-type non-Abelian anyons, and how they can be overcome using Fibonacci anyon models.

To conclude this review of different models, we have explored some regions of the three-dimensional phase diagram for the parafermion model with two extensions. We have seen how it is very likely that the critical surface separating the trivial and $\mathbb{Z}_3$-ordered topological phases is characterised by a Potts-type conformal field theory with central charge $c = 4/5$, at least for moderate values of the parameters. We have also noticed the presence of a Peschel-Emery line along the parameter space, through which the system is frustration-free, i.e. its energy gap is exactly closed. We have seen how different critical points such as C_1 or C_2 move through the parameter space for different values of V, and how C_1 retains its original Potts-type critical point nature. An open question that has not been analysed in this work is what happens to the critical point C_2 described by a CFT with $c = \frac{8}{5}$ given by the superposition of two Potts-type theories, as well as to all phases located in the lower half of the phase diagram for $f \leq 0$.

It is worth noting that the procedures given in this work are potentially generalisable to a much wider range of models. To demonstrate this, a further one-dimensional quantum system, given by a Hamiltonian interpolated between the quantum torus chain and the Sutherland model, was approached using the same approach and techniques that were applied to the other models in this thesis. This allowed us to calculate some of its properties, such as the probable closure of its energy gap and the value of its central charge, as shown in Appendix A.

8.1 Possible extensions

There are many possible extensions to this thesis, just as there are many possible extensions to the models discussed in it. However, in this section we will review some of the more obvious extensions that were considered during the course of the thesis.

The first of these extensions is the generalisation of the real 3-state Potts model to include chiral effects. It is known that the chiral Potts model exhibits strong edge modes, i.e. they are present throughout the spectrum of the system and not just in the ground state. This would require the consideration of complex parameters, which practically implies the introduction of additional angular parameters in the form of pure phases as shown in the Hamiltonian 5.6. For example, in the case of the extended ANNNP model given by the formula 7.1, its chiral extension would correspond to a Hamiltonian of the form

$$H = -Je^{-i\theta_J}\sum_{j=1}^{L-1}\sigma_j\sigma_{j+1}^{\dagger} - fe^{-i\theta_j}\sum_{j=1}^{L}\tau_j + Ue^{-i\theta_U}\sum_{j=1}^{L-1}\tau_j\tau_{j+1} + Ve^{-i\theta_V}\sum_{j=1}^{L-1}\tau_j\tau_{j+1}^{\dagger}. \tag{8.1}$$

The second of these extensions would be to perform a similar analysis but for the set of phases found in the lower half of the diagram 6.1. These phases, which have been extensively evaluated in [1] and which have been described as 'exotic' in Figures 7.9, 7.10 and 7.11, may undergo analogous changes to the trivial and topological phase when the parameter V is changed. For example, it is not known whether the critical point C_2 retains its properties, such as being described by two copies of the Potts model and a central charge $c = 8/5$ for a finite value of V.

Thirdly, it may be possible to analyse two-dimensional phase diagrams similar to that shown by 6.1 within the three-dimensional space (f, U, V). This would give us a better understanding of the three-dimensional phase space of this model and thus its properties. This exploration can be done in conjunction with the representation of a wider range of parameter values. For example, asymptotic cases where one parameter is taken to be much larger than the rest can be considered. Such an exploration is easily done by rough topographies of the central charge and/or entanglement entropy, as was done in Figure 7.1 or 7.2 to fit a critical surface. In Appendix 2 we see some of the results of this approach which, although not relevant to the analysis carried out for this work, provides an interesting insight into the structure of the 7.1 model for a wider set of parameters. Of particular interest is the cut in the UV-plane for large values of both parameters, as it appears to contain an ample collection of topological phases as seen in Figure B.2 in Appendix B.

A | Study of a parametric interpolation between the Sutherland and the quantum torus chain models

Although in this work we have focused on the study of parafermion chains with extensions, it is possible to apply the same approach to other categories of strongly correlated quantum systems. In fact, during the development of this work we had the opportunity to analyse an alternative model using the same methods.

The model in question is an interpolation between the well-known Sutherland model and a more recent model called the quantum torus chain. It is possible to postulate a parametrized Hamiltonian in terms of a θ parameter that bridges both models along its parametric trajectory. It is expected that it may be possible to analyse the quantum torus chain by matching it to the Sutherland model via the interpolation Hamiltonian, provided it has the appropriate properties.

In this appendix we carry out an analysis of the model using the same methods as those used to study parafermion chains, using the numerical methods DMRG and MERA.

A.1 Introduction

The Sutherland model is the name given to a spin chain introduced by B. Sutherland in 1975 where the symmetry group obeyed by each local Hilbert space is $SU(3)$ [47]. This model is quite similar to the 3-state Potts model in that each of the spins can take three different values, although the symmetry group is different. It is a model that has been widely analyzed in the literature. Its Hamiltonian is given by

$$H_{SU} = \sum_j P_{j,j+1}, \tag{A.1}$$

where P_{jj+1} is a swap operator that acts on the basis states as

$$P_{j,j+1} |n, m\rangle = |m, n\rangle . \tag{A.2}$$

This operator can be rewritten in terms of the τ and σ 5.2 matrices introduced in Chapter 5 to describe the 3-state Potts model, in the form:

$$\begin{aligned} P_{j,j+1} =& \frac{1}{3}\left(1+\tau_j^\dagger\tau_{j+1}+\tau_j\tau_{j+1}^\dagger\right) \\ &+\frac{1}{3}\sigma_j^\dagger\sigma_{j+1}\left(1+\omega^2\tau_j^\dagger\tau_{j+1}+\omega\tau_j\tau_{j+1}^\dagger\right) \\ &+\frac{1}{3}\sigma_j\sigma_{j+1}^\dagger\left(1+\omega\tau_j^+\tau_{j+1}+\omega^2\tau_j\tau_{j+1}^\dagger\right). \end{aligned} \tag{A.3}$$

On the other hand, the quantum torus chain is a category of quantum models introduced in 2012 by Qin et al [48]. It is characterised by a discrete global symmetry but on-site projective representations. It also has a parameter that controls the presence or absence of frustration. Again, this model can be written in terms of the matrices τ and σ as

$$H_{QT}(\alpha) = \sum_j \left(\cos\alpha\cdot\tau_j\tau_{j+1}^\dagger + \sin\alpha\cdot\sigma_j^\dagger\sigma_{j+1}\right) + \text{ H.c..} \tag{A.4}$$

It is possible to postulate an interpolation between the two models in terms of an angular parameter θ. Indeed, if we define the terms

$$H_1 = \sum_j \left(\tau_j^\dagger\tau_{j+1}+\tau_j\tau_{j+1}^\dagger+\sigma_j^\dagger\sigma_{j+1}+\sigma_j\sigma_{j+1}^\dagger\right) \tag{A.5}$$

$$H_2 = \sum_j \left(\omega^2\sigma_j^\dagger\tau_j^\dagger\sigma_{j+1}\tau_{j+1}+\omega^2\sigma_j\tau_j\sigma_{j+1}^\dagger\tau_{j+1}^\dagger+\omega\sigma_j\tau_j^\dagger\sigma_{j+1}^\dagger\tau_{j+1}+\omega\sigma_j^\dagger\tau_j\sigma_{j+1}\tau_{j+1}^\dagger\right) \tag{A.6}$$

then it can be shown how by postulating the Hamiltonian

$$H(\theta) = \cos\theta\cdot H_1 + \sin\theta\cdot H_2, \tag{A.7}$$

we obtain the Sutherland model as a particular case for $\theta = \frac{\pi}{4}$ and the quantum torus chain for $\theta = 0$:

$$\begin{aligned} H(0) &= H_1 = \sqrt{2}H_{QT}\left(\frac{\pi}{4}\right) \\ H\left(\frac{\pi}{4}\right) &= \frac{1}{\sqrt{2}}\left(H_1+H_2\right) = \frac{3}{\sqrt{2}}\left(H_{SU}-\frac{L}{3}\right). \end{aligned} \tag{A.8}$$

Furthermore, when $\theta = \frac{\pi}{4}$, the model becomes the ferromagnetic Sutherland model, characterised by a trivial ground state and given by $|0,0,\cdots,0\rangle$ with energy density $e_{gs} = -\sqrt{2}$.

Therefore we are interested in analysing the interpolating Hamiltonian A.7 for values of θ between 0 and $\frac{\pi}{4}$. In particular, we want to check numerically whether both models have the same underlying conformal field theory. To do this we will check the values of the central charge, the energy gap and the scaling dimensions.

A.2 Results

A.2.1 Central charge

We start by looking at the central charge of the interpolating Hamiltonian A.7 for θ between 0 and $\pi/4$. It is known that the value of the central charge of the CFT associated with the Sutherland model is given by $c = 2$. Since it is greater than unity, this CFT is not a minimal model and is therefore not uniquely characterised by the value of c, nor by the value of its scaling dimensions.

On the other hand, the value of the central charge for the quantum torus chain is not so well known, although it is also expected that $H_{QT}\left(\frac{\pi}{4}\right)$ has a central charge $c = 2$.
Next, in Figure A.1 we show the values obtained for the central charge using the Calabrese-Cardy formula 3.8.

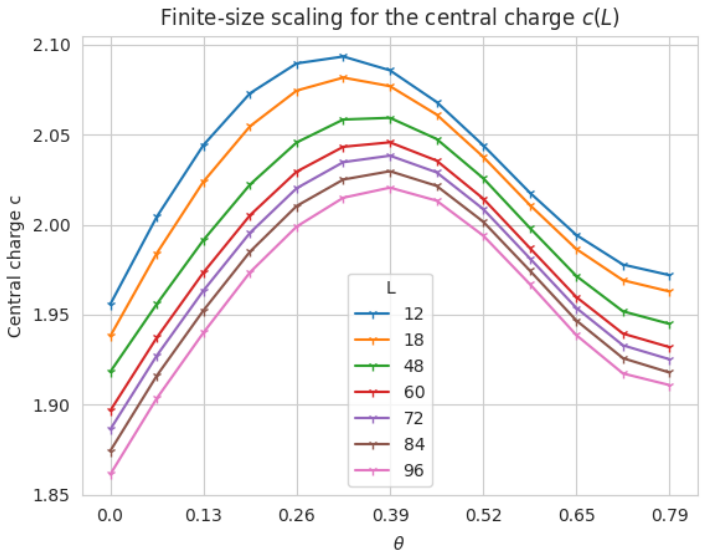

Figure A.1: Central charges

We can see that we find values of the central charge around $c = 2$ for all values of θ, although it shows some noticeable oscillations. These oscillations may be due to finite size effects caused by L, but this result suggests that it is possible for both models to share the same CFT.

A.2.2 Energy gap

On the other hand, we can consider the value of the gap for the A.7 model for different values of θ. It is known that the Sutherland model has no gap, and in the case that the gap remains closed for all values of θ it may indicate that the interpolating Hamiltonian has a common phase between the two points $\theta = 0$ and $\theta = \pi/4$.

In Figure A.2 we show the gap obtained using DMRG, while in Figure A.3 we show the convergence of the gap to zero with respect to the system size, plotting Δ against $1/L$.

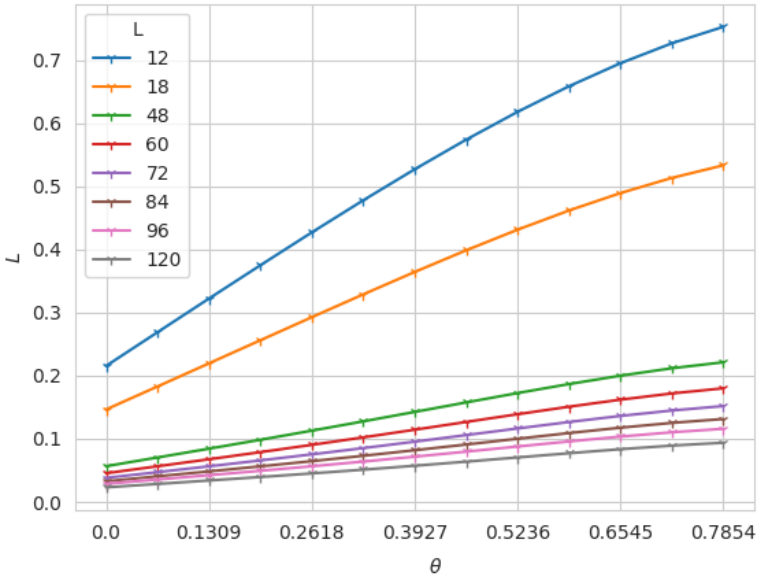

Figure A.2: Energy gap

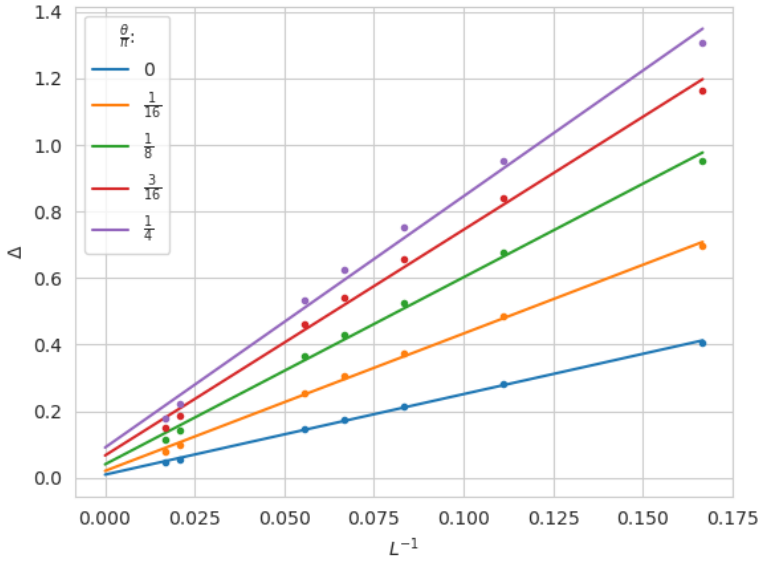

Figure A.3: Convergence of the energy gap as a function of L^{-1}

We can see how the values obtained suggest that the gap between the two points closes.

A.2.3 Correlations

We can also compute the value of the correlation of two operators, in this case $\langle \sigma, \sigma^\dagger \rangle$, using DMRG, although it is not possible to interpret the result as well as the central

charge or the energy gap. The results are shown in Figure A.4

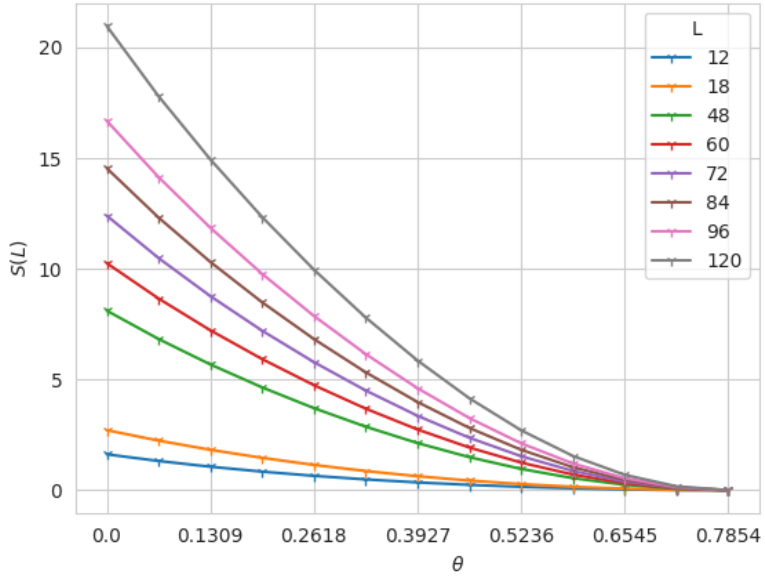

Figure A.4: Operator correlations

We see how the correlation values converge to 0 for the quantum torus chain, while they appear to diverge as a function of L for the Sutherland model.

A.2.4 Scaling dimensions

Since one of the aims is to check whether the CFTs underlying the Sutherland model A.1 and the quantum torus chain A.4 are the same, it may be interesting to compare the values of their scaling dimensions using MERA. However, we stress again that in this case this criterion is not as clear as for parafermion chains, since these theories are not minimal models, their central charge is $c > 1$ and therefore they do not have a limited number of primary fields or scaling dimensions, nor do we know their analytical values. This makes it difficult to obtain and analyse this kind of conformal information.

Nevertheless, we proceed to calculate the values of the first 20 scaling dimensions Δ_k of the interpolation Hamiltonian as a function of θ. We can see the results in Figure A.5.

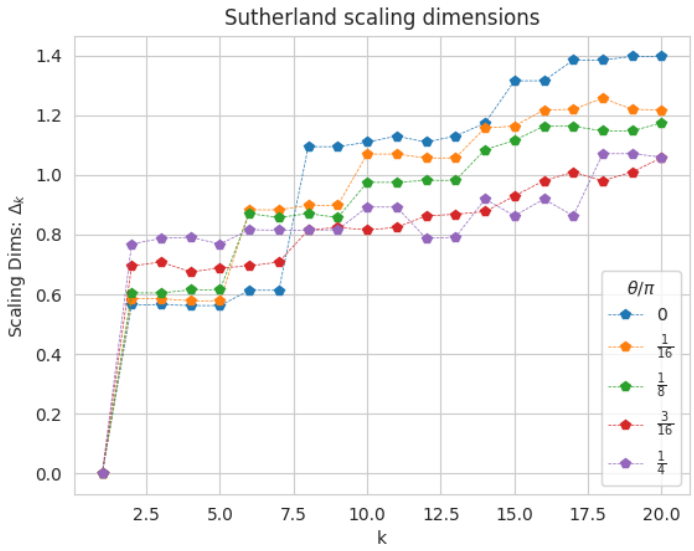

Figure A.5: Scaling dimensions

We see how the result obtained is much more fuzzy than for the parafermion chains. However, we can distinguish some features such as the existence of different structures in terms of the values of θ.

A.2.5 Symmetry

Finally, we show that the interpolation Hamiltonian exhibits angular symmetry with respect to the angle θ around $\theta = \frac{\pi}{4}$. To do this, we compute the central charge roughly by fitting the Calabrese-Cardy formula using a single value of L for $L = 120$, since we are interested in the relative change and not its actual value.

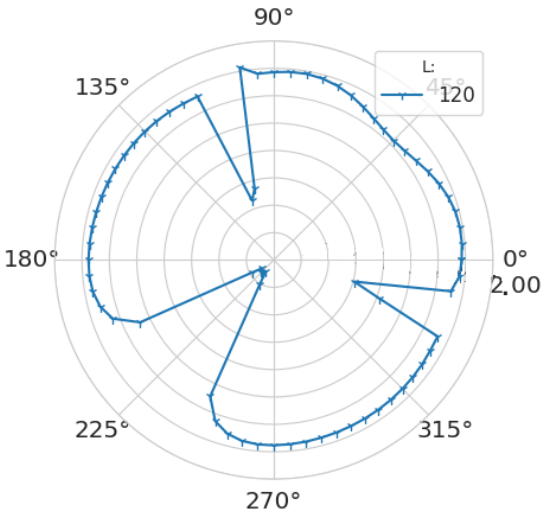

Figure A.6: Symmetry of the central charges

By this symmetry, which has to be proved analytically, we can distinguish as stationary

points the Sutherland model at $\theta = \pi/4$ and the ferromagnetic Sutherland model at $\theta = 5\pi/4$ (which has a central charge $c = 0$ because its ground state is trivial and does not show scale invariance). On the other hand, the quantum torus chain at $\theta = 0$ is mapped to $\theta = \pi/2$. It is apparent that the points at approximately $\theta = -\pi/8$ and $\theta = 5\pi/8$ have a different central charge than the rest of the model and may exhibit different properties.

A.3 Discussion

In this appendix we have analysed the interpolating Hamiltonian between two strongly correlated quantum models, such as the Sutherland model A.1 and the quantum torus chain A.4, in terms of an angular parameter θ. This allows us to demonstrate the applicability of the methods demonstrated for parafermion chains to other systems, and to observe numerically some of the properties of this system.

B | Out-of-scope numerical data

In this Appendix, we report some of the numerical data that is beyond the scope of this thesis, mainly because it corresponds to larger parameter ranges than those required to represent small perturbations with respect to the V term. In particular, we consider here the rough topographies for the central charge and entanglement entropy obtained for planes other than the fU plane, and for V between -2 and 2.

First, a quick scan for the fV plane yields the results shown in Figs. B.1(a) and (b). We can see that at $U = 0$ the critical surface takes a similar shape to that seen for the fU plane and no new phases seem to emerge. Therefore, one would expect the critical surface to separate the same phases as before and also to be of the Potts type. It would be interesting to fit a surface to these data to extend the one found for the fU plane.

On the other hand, if we perform the same procedure for the UV plane, taking the value $f = 0$, we obtain a much more complex and intriguing topography, as can be seen in Figs. B.2 (a) and (b). One can see at a glance the emergence of a collection of topological phases and quantum phase transitions. The phase corresponding to the large central region is expected to be the standard $\mathbb{Z}_3$ ordered topological phase. At the same time, it appears that this phase is surrounded by several transitions at its boundaries. It is likely that many of these transitions correspond to the phases given for the lower half of the diagram in the fU plane for $f \leq 0$. A better understanding of the phases for such slices of the three-dimensional phase diagram may lead to a better understanding of extended parafermion models and their topological properties.

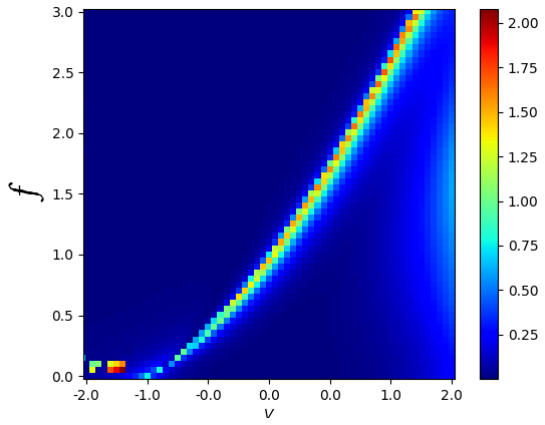

(a) Central charges

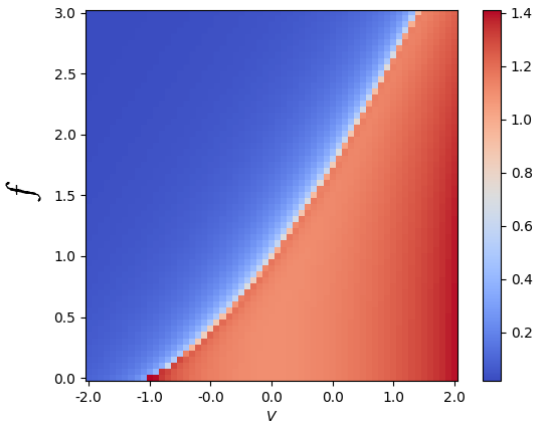

(b) Entanglement entropy

Figure B.1: Rough topography at the fV plane for $U = 0$.

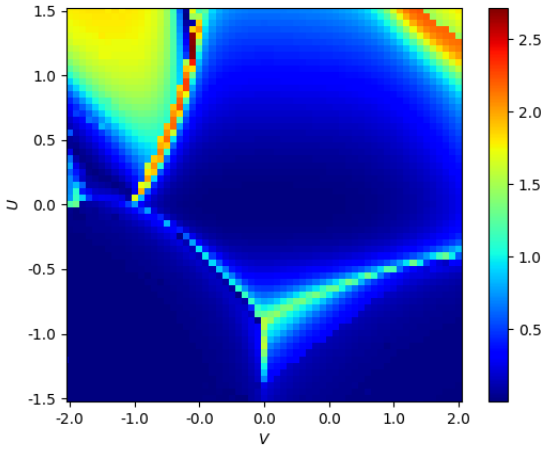

(a) Central charges

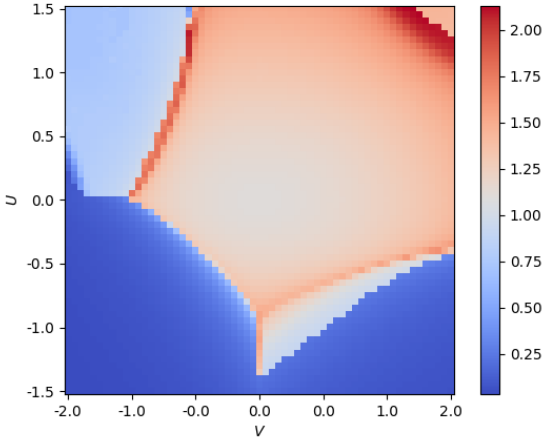

(b) Entanglement entropy

Figure B.2: Rough topography at the UV plane for $f = 0$.

Bibliography

[1] J. Wouters, F. Hassler, H. Katsura, and D. Schuricht, "Phase diagram of an extended parafermion chain," *SciPost Physics Core*, vol. 5, no. 1, p. 008, 2022.

[2] A. M. Turing *et al.*, "On computable numbers, with an application to the entscheidungsproblem," *J. of Math*, vol. 58, no. 345-363, p. 5, 1936.

[3] J. Bardeen and W. H. Brattain, "The transistor, a semi-conductor triode," *Physical Review*, vol. 74, no. 2, p. 230, 1948.

[4] R. De Wolf, "Quantum computing: Lecture notes," *arXiv preprint arXiv:1907.09415*, 2019.

[5] R. P. Feynman, "Simulating physics with computers," in *Feynman and computation*, pp. 133–153, CRC Press, 2018.

[6] P. W. Shor, "Polynomial-time algorithms for prime factorization and discrete logarithms on a quantum computer," *SIAM review*, vol. 41, no. 2, pp. 303–332, 1999.

[7] D. Aharonov and M. Ben-Or, "Fault-tolerant quantum computation with constant error," in *Proceedings of the twenty-ninth annual ACM symposium on Theory of computing*, pp. 176–188, 1997.

[8] S. Trebst, M. Troyer, Z. Wang, and A. W. Ludwig, "A short introduction to fibonacci anyon models," *Progress of Theoretical Physics Supplement*, vol. 176, pp. 384–407, 2008.

[9] L. Savary and L. Balents, "Quantum spin liquids: a review," *Reports on Progress in Physics*, vol. 80, no. 1, p. 016502, 2016.

[10] M. Z. Hasan and C. L. Kane, "Colloquium: topological insulators," *Reviews of modern physics*, vol. 82, no. 4, p. 3045, 2010.

[11] S. M. Young and C. L. Kane, "Dirac semimetals in two dimensions," *Physical review letters*, vol. 115, no. 12, p. 126803, 2015.

[12] M. Sato and Y. Ando, "Topological superconductors: a review," *Reports on Progress in Physics*, vol. 80, no. 7, p. 076501, 2017.

[13] "Online course on topology in condensed matter." `https://topocondmat.org/`.

[14] P. Ginsparg, "Applied conformal field theory," *arXiv preprint hep-th/9108028*, 1988.

[15] D. Tong, "Lectures on string theory," *arXiv preprint arXiv:0908.0333*, 2009.

[16] J. Cardy, *Scaling and renormalization in statistical physics*, vol. 5. Cambridge university press, 1996.

[17] A. B. Zamolodchikov, "Irreversibility of the flux of the renormalization group in a 2d field theory," *JETP lett*, vol. 43, no. 12, pp. 730–732, 1986.

[18] "Introduction to exact diagonalization." https://indico.ictp.it/event/a14246/session/31/contribution/51/material/0/0.pdf.

[19] R. Penrose, "Applications of negative dimensional tensors," *Combinatorial mathematics and its applications*, vol. 1, pp. 221–244, 1971.

[20] R. Orús, "A practical introduction to tensor networks: Matrix product states and projected entangled pair states," *Annals of physics*, vol. 349, pp. 117–158, 2014.

[21] J. Hauschild and F. Pollmann, "Efficient numerical simulations with tensor networks: Tensor network python (tenpy)," *SciPost Physics Lecture Notes*, p. 005, 2018.

[22] P. Calabrese and J. Cardy, "Entanglement entropy and conformal field theory," *Journal of physics a: mathematical and theoretical*, vol. 42, no. 50, p. 504005, 2009.

[23] R. Samajdar, S. Choi, H. Pichler, M. D. Lukin, and S. Sachdev, "Numerical study of the chiral z 3 quantum phase transition in one spatial dimension," *Physical Review A*, vol. 98, no. 2, p. 023614, 2018.

[24] C. Hamer, J. B. Kogut, and L. Susskind, "Strong-coupling expansions and phase diagrams for the o (2), o (3), and o (4) heisenberg spin systems in two dimensions," *Physical Review D*, vol. 19, no. 10, p. 3091, 1979.

[25] G. Evenbly and G. Vidal, "Quantum criticality with the multi-scale entanglement renormalization ansatz," pp. 99–130, 2013.

[26] "Example codes: variational mera." https://www.tensors.net/mera.

[27] R. N. Pfeifer, G. Evenbly, and G. Vidal, "Entanglement renormalization, scale invariance, and quantum criticality," *Physical Review A*, vol. 79, no. 4, p. 040301, 2009.

[28] A. Y. Kitaev, "Unpaired majorana fermions in quantum wires," *Physics-uspekhi*, vol. 44, no. 10S, p. 131, 2001.

[29] E. Majorana and L. Maiani, "A symmetric theory of electrons and positrons," *Ettore Majorana Scientific Papers: On occasion of the centenary of his birth*, pp. 201–233, 2006.

[30] E. Lieb, T. Schultz, and D. Mattis, "Two soluble models of an antiferromagnetic chain," *Annals of Physics*, vol. 16, no. 3, pp. 407–466, 1961.

[31] P. Calabrese, F. H. Essler, and M. Fagotti, "Quantum quench in the transverse field ising chain: I. time evolution of order parameter correlators," *Journal of Statistical Mechanics: Theory and Experiment*, vol. 2012, no. 07, p. P07016, 2012.

[32] I. Mahyaeh and E. Ardonne, "Zero modes of the kitaev chain with phase-gradients and longer range couplings," *Journal of Physics Communications*, vol. 2, no. 4, p. 045010, 2018.

[33] J. Alicea, "New directions in the pursuit of majorana fermions in solid state systems," *Reports on progress in physics*, vol. 75, no. 7, p. 076501, 2012.

[34] D. J. Clarke, J. Alicea, and K. Shtengel, "Exotic non-abelian anyons from conventional fractional quantum hall states," *Nature communications*, vol. 4, no. 1, p. 1348, 2013.

[35] M. Deng, C. Yu, G. Huang, M. Larsson, P. Caroff, and H. Xu, "Anomalous zero-bias conductance peak in a nb–insb nanowire–nb hybrid device," *Nano letters*, vol. 12, no. 12, pp. 6414–6419, 2012.

[36] R. M. Lutchyn, E. P. Bakkers, L. P. Kouwenhoven, P. Krogstrup, C. M. Marcus, and Y. Oreg, "Majorana zero modes in superconductor–semiconductor heterostructures," *Nature Reviews Materials*, vol. 3, no. 5, pp. 52–68, 2018.

[37] F. Hassler and D. Schuricht, "Strongly interacting majorana modes in an array of josephson junctions," *New Journal of Physics*, vol. 14, no. 12, p. 125018, 2012.

[38] H. Katsura, D. Schuricht, and M. Takahashi, "Exact ground states and topological order in interacting kitaev/majorana chains," *Physical Review B*, vol. 92, no. 11, p. 115137, 2015.

[39] I. Peschel and V. Emery, "Calculation of spin correlations in two-dimensional ising systems from one-dimensional kinetic models," *Zeitschrift für Physik B Condensed Matter*, vol. 43, no. 3, pp. 241–249, 1981.

[40] R. B. Potts, "Some generalized order-disorder transformations," in *Mathematical proceedings of the cambridge philosophical society*, vol. 48, pp. 106–109, Cambridge University Press, 1952.

[41] P. Fendley, "Parafermionic edge zero modes in zn-invariant spin chains," *Journal of Statistical Mechanics: Theory and Experiment*, vol. 2012, no. 11, p. P11020, 2012.

[42] E. Fradkin and L. P. Kadanoff, "Disorder variables and para-fermions in two-dimensional statistical mechanics," *Nuclear Physics B*, vol. 170, no. 1, pp. 1–15, 1980.

[43] E. Stoudenmire, D. J. Clarke, R. S. Mong, and J. Alicea, "Assembling fibonacci anyons from a z 3 parafermion lattice model," *Physical Review B*, vol. 91, no. 23, p. 235112, 2015.

[44] N. H. Lindner, E. Berg, G. Refael, and A. Stern, "Fractionalizing majorana fermions: Non-abelian statistics on the edges of abelian quantum hall states," *Physical Review X*, vol. 2, no. 4, p. 041002, 2012.

[45] I. Mahyaeh and E. Ardonne, "Exact results for a z 3-clock-type model and some close relatives," *Physical Review B*, vol. 98, no. 24, p. 245104, 2018.

[46] J. Wouters, H. Katsura, and D. Schuricht, "Interrelations among frustration-free models via witten's conjugation," *SciPost Physics Core*, vol. 4, no. 4, p. 027, 2021.

[47] B. Sutherland, "Model for a multicomponent quantum system," *Physical Review B*, vol. 12, no. 9, p. 3795, 1975.

[48] M. Qin, J. M. Leinaas, S. Ryu, E. Ardonne, T. Xiang, and D.-H. Lee, "Quantum torus chain," *Physical Review B*, vol. 86, no. 13, p. 134430, 2012.